



## Near-bed turbulence and relict waveformed sand ripples: Observations from the inner shelf

Alex E. Hay<sup>1</sup>

Received 11 November 2006; revised 27 September 2007; accepted 20 December 2007; published 30 April 2008.

[1] Results are presented from a field investigation of near-bed turbulence above degrading waveformed sand ripples in 17-m water depth on the inner shelf. The heights of the 50-cm wavelength primary ripples were about 5 cm at the start of the observation period, and decreased by a factor of 2 within 15 days. The principal degradation mechanism involved fish making pits in the seafloor. Near-bed turbulent kinetic energy dissipation rates are estimated both from the energy spectrum and from the vertical structure function within the inertial subrange, and ranged from  $0.1 \times 10^{-6}$  to  $3 \times 10^{-6}$  W/kg. The friction velocity,  $u_*$ , at the bed ranged from 0.3 to 0.5 cm/s, and the wave friction factor,  $f_w$ , from 0.017 to 0.02. The nearbed turbulence intensities and consequently the estimated values of  $u_*^2$  and  $f_w$  are likely too small by a factor of 2, partly to satisfy the smooth-wall constraint, and partly to account for the effects of small-scale turbulence within the finite-volume range cells of the coherent Doppler system used to make the turbulence estimates. Finally, the results indicate that the hydraulic roughness of relict ripples is likely a function of both ripple height and steepness, and that the relative roughness should also depend on the near-bed wave orbital excursion. For modeling purposes, Nielsen's ripple roughness formula is recommended, with a reduced proportionality constant to account for the effects of irregular wave forcing and non-equilibrium ripple history.

**Citation:** Hay, A. E. (2008), Near-bed turbulence and relict waveformed sand ripples: Observations from the inner shelf, *J. Geophys. Res.*, 113, C04040, doi:10.1029/2006JC004013.

### 1. Introduction

[2] Waveformed ripples are a common seabed feature in sandy sediments on the continental shelf. Such ripples present a bottom roughness field to the overlying fluid which is both highly anisotropic and temporally variable. While the effects of ripple roughness on low-frequency currents are known to be important [Grant and Madsen, 1986], and ripple-induced friction is central to the transport of mobile seafloor sediments [Sleath, 1984; Fredsoe and Deigaard, 1992; Nielsen, 1992], much of the work on ripple properties has focused on active transport conditions. However, the largest fraction of the time-history of a ripple field could easily be spent in the relict state: that is, in the weeks or months following the relatively brief period of formation during a storm event.

[3] Recent comparisons between observed and model-predicted wave energy gradients on broad shallow shelves indicate that relict ripples can contribute significantly to wave energy dissipation [Ardhuin *et al.*, 2003a, 2003b]. Recent work has also shown that sound incident on the seabed at sub-critical grazing angles can penetrate more deeply into the bottom when ripples are present [Thorsos *et*

*al.*, 2001]. This result has implications for buried object detection, and questions related to ripple persistence are highly relevant.

[4] Very little is known about the relict bed state, however. The outstanding questions include: (a) what are the rates of ripple decay? (b) what are the relative importance of physical and biological mechanisms leading to ripple decay? (c) how is the spectrum of bottom roughness affected by decay? (d) what is the effective hydraulic roughness of a relict ripple field? (e) what model or models can be used to suitably represent the decay process? The first four of these questions are addressed in the present paper. The last will be treated elsewhere.

[5] The observations presented here are from a field experiment carried out in the northeastern Gulf of Mexico during the autumn. Given that autumnal storms in this region occur at intervals of several weeks, the idea was that the lengthy periods of relative calm between storm events would provide opportunities for investigating flow and turbulence over relict ripples. Also, the instrument pod was expected to serve as refuge for fish, and thereby result in higher rates of biological reworking of the sediments and therefore to accelerated rates of ripple decay. As will be shown, both of these expectations were met. In addition, however, this region is occasionally visited by hurricanes. Several weeks prior to the measurement period discussed here, Hurricane Ivan made landfall 100 km to the west of the experiment site. The waves generated by this upper

<sup>1</sup>Department of Oceanography, Dalhousie University, Halifax, NS, Canada.

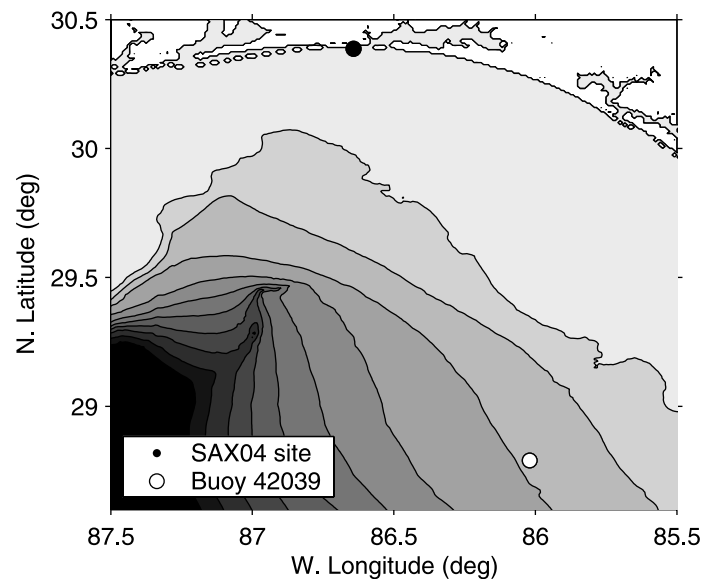


**Figure 1.** Location of the SAX04 study site relative to the large-scale bathymetry and coastline in the northeastern Gulf of Mexico. The location of NDBC buoy 42039 is also shown. Contour interval is 100 m.

category 3 event reached heights of 15-m offshore in 200-m depth, and resulted in significant remobilization of the seabed sediments at the experiment site. It is likely that the remobilization was sufficiently intense that much of the benthic infauna were destroyed, effectively resetting the benthic ecosystem clock to time zero.

[6] The paper is organized as follows. The experimental and analysis methods, including a brief description of the experiment site, are outlined in section 2. The main experimental results are presented in three separate sections, in the following order: Section 3 summarizes the background hydrodynamic forcing and near-bed turbulence, including dissipation rates; section 4 the ripple characteristics, including a brief summary of biological re-working of the surficial sediments, most notably by fish; and section 5 the bottom friction results. In the Discussion, section 6, the observed dissipation rates and friction factor estimates are compared to previous results, and the effects of phase noise on the turbulence intensity measurements examined. The main results and conclusions of the study are summarized in section 7.

## 2. Methods

### 2.1. Experiment Site

[7] SAX04 (Sediment Acoustics Experiment 2004) was carried out on the west Florida shelf in the northeastern Gulf of Mexico, approximately 2 km from the shoreline in 17-m mean water depth (Figure 1), as a follow-up to a previous sediment acoustics experiment, SAX99, at nearly the same location in 1999. Results from SAX99, including information about the study area, may be found in *Thorsos et al.* [2001] and *Richardson et al.* [2001], and in a special issue of the *Journal of Oceanic Engineering* [see *Thorsos and Richardson*, 2002]. As a similar special issue is being planned for SAX04, the following brief description of the site is limited to only the most relevant points.

[8] The experiment ran from 26 September to 2 November 2004. As in 1999, the R/V *Seward Johnson* was four-point moored on site, serving as the data acquisition and support platform for a range of experiments. The results presented here are from Dalpod1, which was deployed 140 m due east of the vessel. Armored cables for communications and power ran along the bottom from the pod to the ship. Being so close to shore, the R/V *Seward Johnson* could not remain connected to the mooring when the wind speed or sea state reached levels that would endanger the vessel were the mooring to fail. Thus there were times during the experiment when the ship had to disconnect from the mooring, leading to gaps in the data record. The results presented here are for a 19-d period following Tropical Storm Matthew, a significant weather event which in addition to creating new ripples on the seafloor forced the ship to leave the mooring for 4 days. As a result of this disconnection, and also the loss of autonomous wave-recording instruments deployed as part of SAX04 (but prior to the passage of Hurricane Ivan through the area on 16 September), measurements of wave conditions at the SAX04 site are not available for TS Matthew. Thus reference is made here to the wave data recorded by the nearest National Buoy Data Center (NDBC) buoy, number 42039, in 291-m water depth (Figure 1).

[9] The bottom sediments at the Dalpod1 location were primarily medium sand. Sieve analysis of 4 samples collected in the immediate vicinity of the frame yielded  $405 \pm 6 \mu\text{m}$  (mean  $\pm$  standard deviation) for  $D_{50}$ ,  $288 \pm 5 \mu\text{m}$  for  $D_{16}$ , and  $560 \pm 15 \mu\text{m}$  for  $D_{84}$ . The subscripts denote percent finer. Following Hurricane Ivan, mud deposits were found on the seabed at the SAX04 site, in patches 5–10 m in lateral extent. No mud deposits were found close to Dalpod1.

[10] Another feature of the experiment, possibly also a consequence of Hurricane Ivan, was a barnacle settlement event in late September. Instrument packages deployed

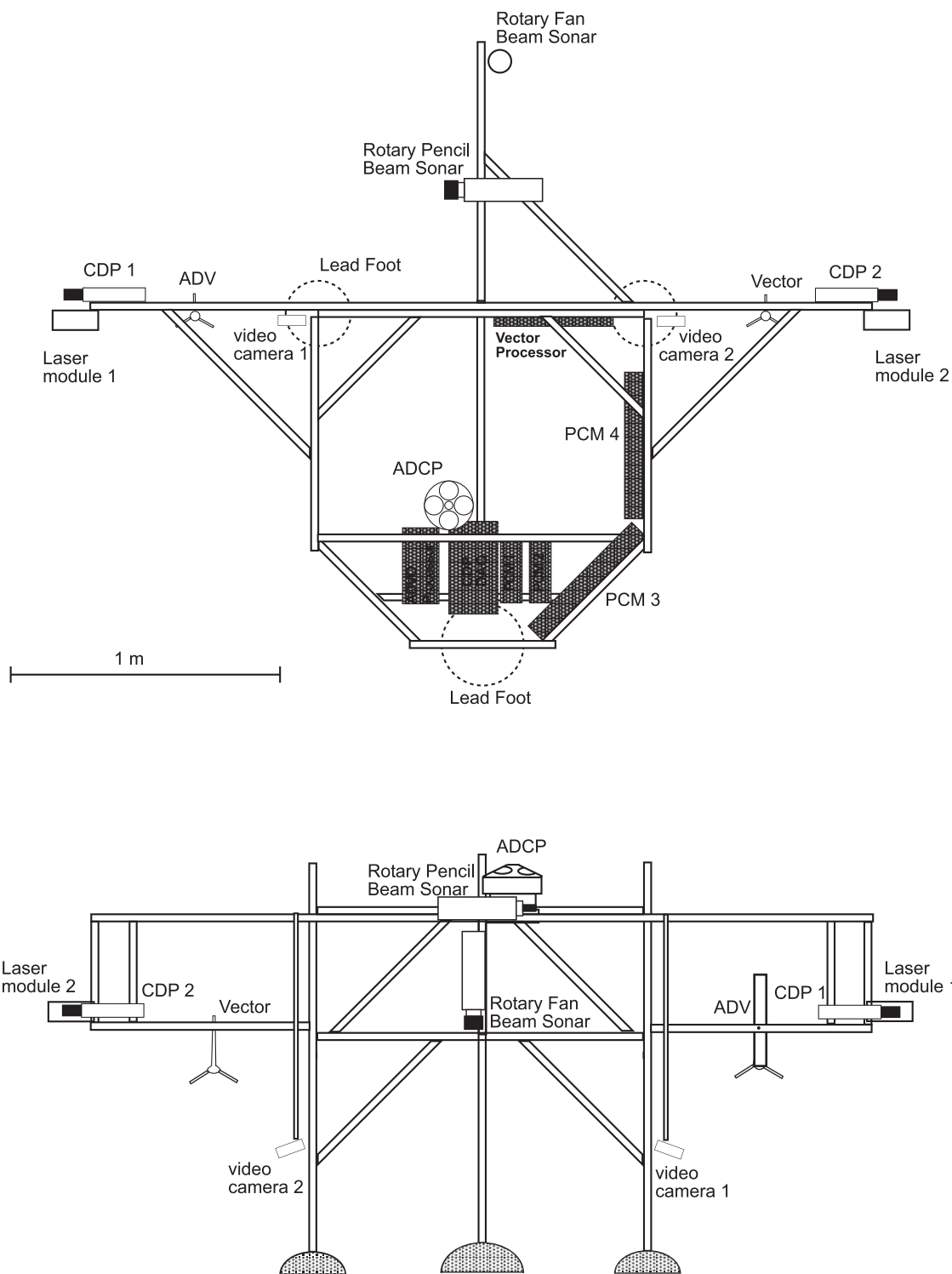


**Figure 2.** Plan and front views of Dalpod1. The seaward direction is toward the top of the page in the plan view, and out of the page in the front view. In the top view, the shaded rectangles represent the housings for the ADV-O and Vector processors, the CDP data acquisition system, and the power and control modules for the rotary sonars (PCM1, PCM2) and the two laser-video systems (PCM3, PCM4). These have been omitted from the front view.

during the week following Ivan’s passage, Dalpod1 included, were heavily colonized by barnacles. As will be seen, the growth of barnacles on sensor surfaces affected the data quality for some Dalpod1 sensors.

**2.2. Instrumentation**

[11] Scale diagrams of Dalpod1 are presented in Figure 2. Constructed from 3-cm diameter galvanized steel pipe, the frame was ballasted at the seabed by two 22-kg feet on the

seaward legs, and a 44-kg foot on the shoreward leg. The feet were made of lead cast into spherical caps, and deployed with the spherical surface uppermost so as to present no sharp edges to the flow. The instruments were mounted on cantilevered arms ca. 1-m in length, extending away from the main body of the frame in the seaward, eastward and westward directions. The cantilevered design was motivated by the dual need to: (a) reduce the possibility of eddies shed from the structure affecting the measurements in the areas of interest; and (b) remove the instruments as far as practically possible from the fish and other organisms which were expected to use the main body of the frame as a refuge. With the duplicate instrument suite on the eastern and western sides, one set of instruments would be on the upstream side of the frame for a given alongshore flow direction.

[12] The two downward-looking single-beam pulse-coherent acoustic Doppler profilers (CDPs, 1.7 MHz, 0.7-cm range bins, 2° half-power beam width [Zedel and Hay, 1999]) operated from 1-m nominal height at an ensemble-averaged profile sampling rate of 21 Hz. Each ensemble comprised 19 pulse pairs, and thus ca. 1-mm/s accuracy for the along-beam velocity [Zedel *et al.*, 1996]. The beams were rotated about the east-west axis at an angle of 5° with respect to vertical in the seaward direction. The purpose of the 5-degree rotation was to minimize interference from multiple reflections. The purpose of the CDPs was to measure near-bed turbulence. The CDP records were about 24-min long, and were acquired every 1/2-h.

[13] An upward-looking, 1.2-MHz RD Instruments Acoustic Doppler Current profiler with RDI's Waves Package firmware was also mounted on the frame. The Waves ADCP acquired ensemble-averaged velocity profiles continuously at 2-min intervals in 0.5-m range cells, with 50 pings per ensemble. The velocity accuracy quoted by the manufacturer for these settings is 0.86 cm/s. Wave data were acquired for 20 min at 2 Hz every 1/2 h, yielding wave directional spectra with 0.0078-Hz resolution in frequency and 4° resolution in azimuth. The instrument generates three different 1-dimensional wave energy spectra, one based on pressure, another on surface elevation determined from the sea surface echo, and the third from the wave orbital velocities at 8-, 10-, and 12-m heights above bottom. The results presented here are from the velocity-based method (expected to more accurate in this water depth).

[14] An acoustic Doppler velocimeter was mounted on each of the two shore-parallel arms, one 5-MHz Sontek ADV-O and one 6-MHz Nortek Vector. The ADV-O data were quite noisy, probably because of incomplete removal of the biofouling, and are not discussed further. The Vector data were also degraded by the biofouling initially, but returned to normal after the transducer faces were scraped clean by divers. The Vector operated at an 8-Hz sampling rate with a 4- $\mu$ s transmit pulse duration and a 30-cm/s maximum velocity setting. Runs were acquired every 1/2-h, each 8192 points or about 17 min in length.

[15] The rotary sonars were 2.25-MHz Mesotech Model 971s. The pencilbeam housing was mounted horizontally as shown in Figure 2, such that the beam axis rotated in a vertical plane oriented in the cross-shore direction. The fanbeam was mounted so that the transducer rotated about a vertical axis, with its beam pattern narrow in azimuth and

broad in the vertical. Further details on these sonars are given by Hay and Mudge [2005] and the papers cited therein. The rotary sonar data were collected hourly. For each data run, 3 consecutive 360-degree scans with an angular resolution of 0.45° were acquired in about 1.5 min. The resolution of the backscatter profile at each angle was 0.6 cm in range, and 16 bits in amplitude.

### 2.3. Data Processing and Analysis

[16] Near-bottom root-mean square (rms) wave orbital velocities,  $\tilde{u}_b$ , were determined from the Vector and the WavesADCP records. Since linear wave theory is expected to apply locally for the wave and water depth conditions of the experiment [Guza and Thornton, 1980], near-bed orbital velocities were computed from the Vector bottom pressure data and from the WavesADCP surface elevation spectra. Comparisons between the 3 estimates of  $\tilde{u}_b$  serve as a data quality check.

[17] For the Vector, the velocity-based measure of  $\tilde{u}_b$  is given by

$$\tilde{u}_b = (\sigma_u^2 + \sigma_v^2)^{1/2}, \quad (1)$$

where  $\sigma_u$  and  $\sigma_v$  represent the square-root of the  $u$  and  $v$  variances in the sea-and-swell band, defined to be 0.05 to 0.3 Hz. These variances were determined from the time series after band-pass filtering, both forward and backward in time, using a 5th-order Butterworth filter with cut-off frequencies of 0.05 and 0.3 Hz. For linear surface gravity waves, the pressure-based measure of  $\tilde{u}_b$  is

$$\tilde{u}_b = g \left[ \int \frac{S_{\tilde{p}\tilde{p}}}{c(k)^2} df \right]^{1/2} \quad (2)$$

[see, e.g., Kundu, 1990], where  $g$  is the gravitational acceleration,  $S_{\tilde{p}\tilde{p}}$  is the power spectral density for the near-bed sea-and-swell pressure with the latter expressed in units of m (i.e.,  $\tilde{p} = p/\rho g$ ),  $f$  is the frequency, and  $c = \omega/k$  is the phase speed. The angular frequency  $\omega$  and wave number  $k$  are related through the dispersion relation,

$$\omega^2 = gk \tanh kh, \quad (3)$$

where  $h$  is the water depth. The spectra were computed using Hanning-windowed 799-point segments with 75% overlap, and thus have 37 equivalent degrees of freedom [Nuttall, 1971]. Velocity statistics and spectra were computed from the Vector records after first discarding data points with correlations <70%.

[18] For the WavesADCP,  $\tilde{u}_b$  was based on the surface elevation power spectral density,  $S_{\tilde{\eta}\tilde{\eta}}$ ,  $\tilde{\eta}$  being the surface elevation, and  $S_{\tilde{\eta}\tilde{\eta}}$  the 1-d spectrum derived from the wave orbital velocities. Thus again invoking linear theory,

$$\tilde{u}_b = \left[ \int S_{\tilde{\eta}\tilde{\eta}} \left( \frac{\omega}{\sinh kh} \right)^2 df \right]^{1/2}. \quad (4)$$

[19] Note that the above relations for  $\tilde{u}_b$  represent RMS estimates: significant orbital velocity amplitudes would be

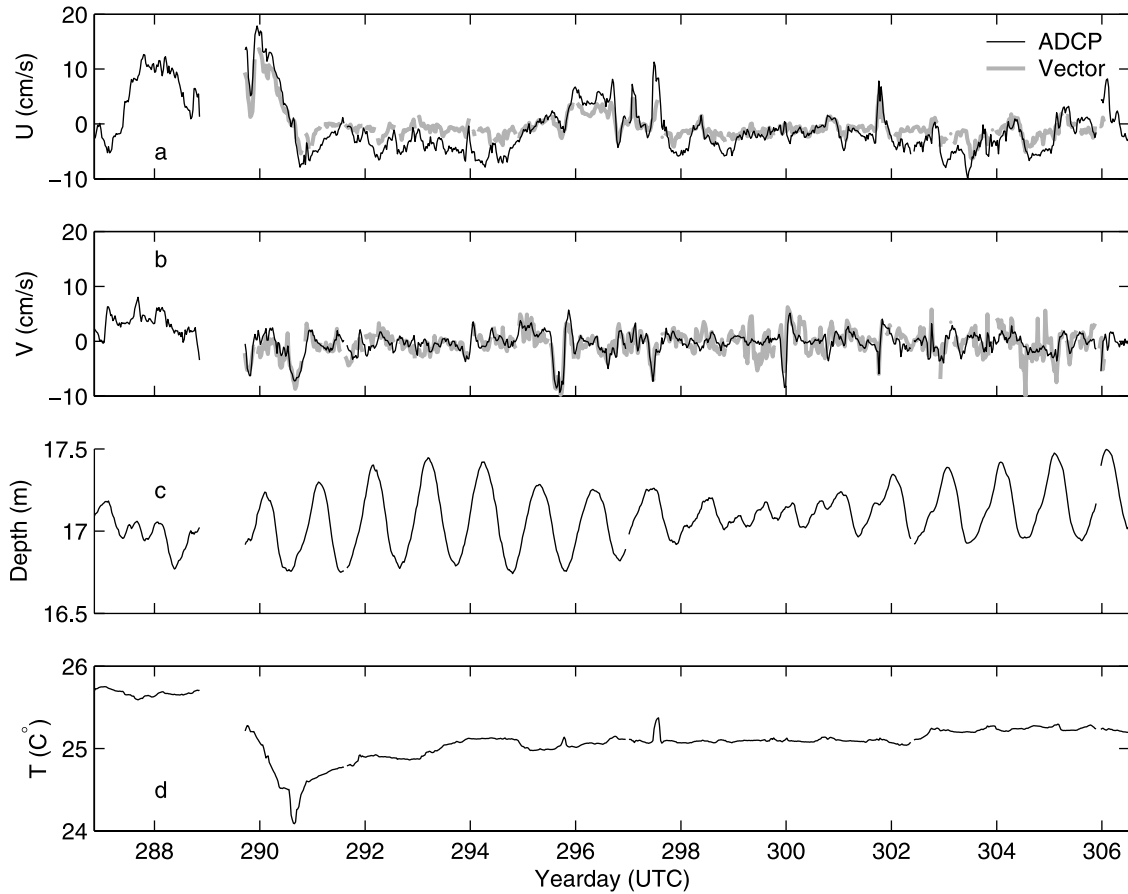


**Figure 3.** Mean near-bottom currents registered by the ADCP (black, 2.5-m height) and the Vector (grey, 0.5-m height): (a)  $U$ , positive eastward; (b)  $V$ , positive northward. (c) Water depth, from ADCP pressure. (d) Water temperature, ADCP. The data start just before midnight on 12 October (Yearday 286).

larger by a factor of 2 [Thornton and Guza, 1983]. The surface elevation variance,  $\sigma_{\eta}^2$ , was obtained by integrating  $S_{\eta\eta}$  over the sea-and-swallow band, and significant wave height,  $H_s$ , defined as  $4\sigma_{\eta}$  [Thornton and Guza, 1983].

[20] The CDP data were first subjected to a 2-pass despiking routine, resulting in an average data discard rate of 2%, and a range of 0.5% to 5%. Vertical velocity spectra,  $S_{ww}$ , were computed from the 24-min CDP records using Hanning-windowed 1000-point segments with 60% overlap, corresponding to 120 equivalent degrees of freedom. The spectra from 17 range bins adjacent to the bottom (i.e., spanning 1.4 to 12.6-cm heights) were averaged together to obtain the final estimates of  $S_{ww}$ .

[21] The turbulent kinetic energy dissipation rate,  $\epsilon$ , was estimated in two ways, both assuming locally isotropic turbulence, and both based on the inertial subrange. Using the expressions given by Tennekes and Lumley [1972, pp. 252–265], the dissipation for unidirectional flows can be expressed as

$$\epsilon_{Sp} = B_w \frac{S_{ww}^{3/2}(f)}{U} f^{5/2}. \quad (5)$$

[22]  $S_{ww}$  is the spectral density in the inertial subrange, and the subscript  $Sp$  denotes this as the spectral method.  $B_w$  is a constant.  $U$  is a horizontal advection speed used to

convert frequency to wave number via Taylor's frozen turbulence hypothesis: i.e., the wave number,  $k = 2\pi f/U$ . Lumley and Terry [1983] derived expressions for the spectrum of isotropic turbulence in random deep-water waves superimposed on a mean current, which Trowbridge and Elgar [2001] modified for near-bed combined wave-current flows. Bryan *et al.* [2003] extended the Lumley and Terry approach to water of arbitrary depth, for the wave-only case. As shown in the Appendix, these three sets of results can be recast in the form of equation (5), with  $U$  set equal to the RMS near-bed wave orbital velocity,  $\tilde{u}_b$ , and with  $B_w \sim 10$  for the wave-dominated case.

[23] The second relation for estimating  $\epsilon$  is based on the vertical velocity structure function,  $D_{11} = \langle (\Delta w)^2 \rangle$ , where  $\Delta w$  is the difference between CDP vertical velocities in different range bins and  $\langle \rangle$  denotes the ensemble average. The subscript 11 indicates that the velocity component being differenced is parallel to the separation vector between the measurement points. In the inertial subrange, assuming local isotropy,  $D_{11}$  is a function solely of the separation and the dissipation, yielding [Monin and Yaglom, 1971, p. 353; Pope, 2000, p. 193]

$$\epsilon_{SF} = \frac{1}{\Delta z} \left[ \frac{\langle (\Delta w)^2 \rangle}{C} \right]^{3/2} \quad (6)$$

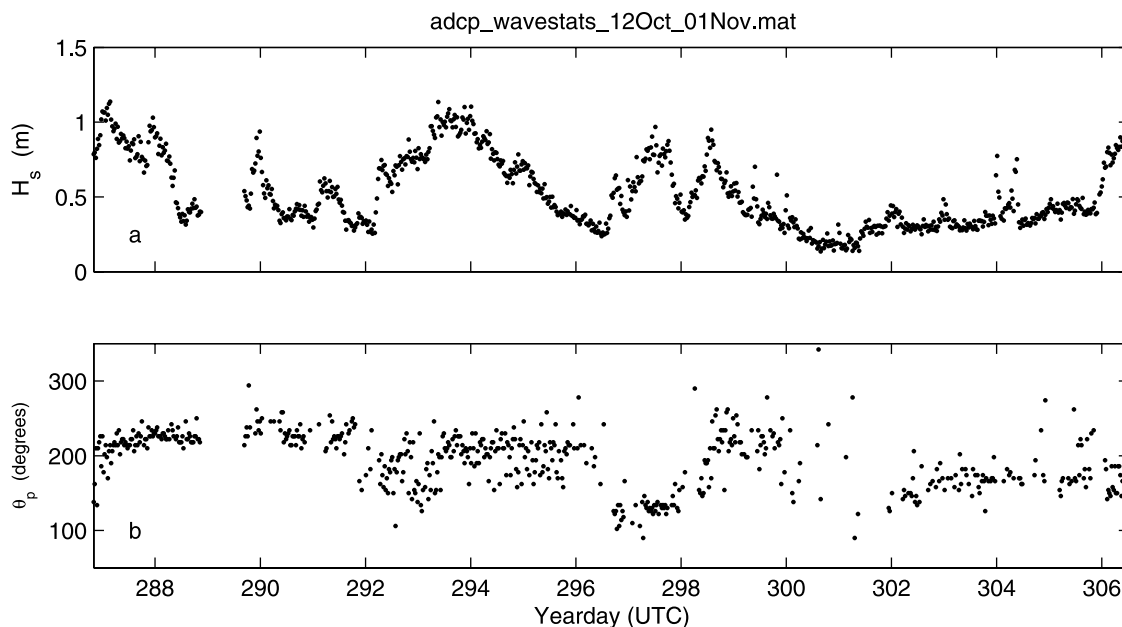


**Figure 4.** Significant wave heights,  $H_s$ , and peak wave directions,  $\theta_p$ , from the ADCP wave directional spectra based on near-surface wave orbital velocities. Directions are relative to north, and indicate the directions from which waves were propagating.

where  $C$  is an empirical constant with a value of 2 [Pope, 2000, p. 194]. To allow for noise in the velocity measurements, this equation is rewritten as

$$\langle(\Delta w)^2\rangle = C[\epsilon_{SF}\Delta z]^{2/3} + \sigma_n^2 \quad (7)$$

where  $\sigma_n^2$  is the noise variance.

[24] Bed elevations were determined from the average of the backscatter amplitude profiles over the 3 consecutive sonar scans. After first locating the maximum amplitude beyond a preset minimum range, the range to the bottom was defined by the amplitude-weighted mean of the points above half maximum. The bed elevation profile as a function of cross-shore distance,  $\eta(y)$ , was computed from the range to the bottom and the known angle of the acoustic beam relative to the vertical at each angular step of the scan. Bed elevation spectra,  $S_{\eta\eta}$  were computed over a 3-m cross-shore distance interval ( $-1.8 \leq y \leq 1.2$  m) using 1.5-m (75-point) Hanning-windowed segments with 66% overlap, yielding spectra with 6 equivalent degrees of freedom. Prior to computing the spectra, the profiles were oversampled at 0.5-cm intervals, low-pass filtered with 50 cpm cutoff, and resampled at 2-cm spacing. Given the  $0.45^\circ$  angular resolution of the data, this spacing corresponds approximately to the maximum achievable cross-shore resolution  $\Delta y$  at the maximum horizontal distance from the sensor along the profile (i.e., 1.8 m here) with the sensor at 1-m height above bottom.

[25] The 3 consecutive fanbeam images were also averaged together for each run. As in previous experiments [see Hay and Mudge, 2005], the backscatter profiles at each azimuth were ranked according to total backscatter (i.e., the backscatter amplitude summed over all range bins) and the profile with the lowest of the 3 values dropped before computing the average. This technique is effective in

removing most of the image contamination associated with shadows cast on the seabed by fish passing through the acoustic beam. The resulting average amplitude image in range-azimuth space was slant-range corrected and interpolated onto a Cartesian  $x, y$  grid with 0.6-cm horizontal spacing.

### 3. Results I: Hydrodynamics

#### 3.1. Currents

[26] Time series of near-bottom currents, water depth, and near-bottom water temperature for the post-Matthew period are presented in Figure 3. The tide was dominantly diurnal, and the tidal range small,  $\sim 0.6$  m maximum. The near-bottom currents exhibit very weak modulation at the diurnal frequency. The mean currents,  $\bar{U}$  and  $\bar{V}$ , over the 19-d duration of the record were small, both equal to  $-0.5$  cm/s at 0.5-m height (Vector data), and equal to  $-0.6$  and  $0.0$  cm/s respectively at 2.5-m height (ADCP). The current variability was dominated by low-frequency ( $>1$ -d period) motions and pulses of a few hours duration, both with amplitudes reaching 10 to 20 cm/s. The low-frequency motions were associated mainly with atmospheric forcing events, one of these resulting in disconnection from the mooring and a consequent break in the data on YD291.

#### 3.2. Waves

[27] Significant wave height,  $H_s$ , and peak wave direction,  $\theta_p$ , are presented in Figure 4. The forcing events appear more clearly in these data. Note in particular the increasing wave heights toward the end of the record, at which point the vessel again disconnected from the mooring. Significant wave heights were typically 1-m maximum. Wave directions were dominantly either from  $\sim 200^\circ$  or  $\sim 150^\circ$  relative to North: i.e., from the southwest or southeast quadrants. Time series of peak wave period,  $T_p$ , are shown in Figure 5.

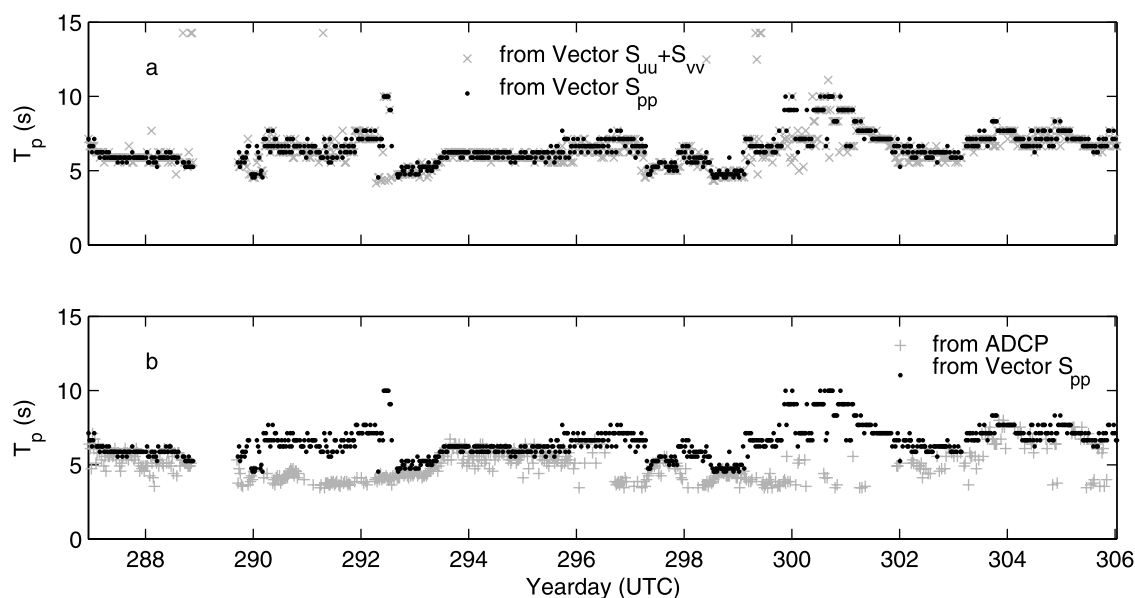


**Figure 5.** Peak wave periods,  $T_p$ : (a) from the Vector pressure and velocity spectra, as indicated; (b) from the ADCP wave orbital velocity spectra and the Vector pressure spectra.

As a data quality check, three different estimates are plotted: values from the Vector pressure spectra,  $S_{pp}$  (solid dots), are compared to values from the Vector velocity spectra,  $S_{uu} + S_{vv}$  (grey cross), in panel (a) and to values from the Waves-ADCP near-surface orbital velocity spectrum (grey plus) in panel (b). The velocity-based values from the Vector are comparable to those based on pressure, but with occasional outliers which are clearly erroneous. The ADCP values are also comparable to the Vector pressure-based estimates, but are typically lower indicating higher peak frequencies, a result of the 17-m water column acting as a low-pass filter for surface gravity waves. Note too that all three estimates tend to be in close agreement when wave heights were larger, and stronger surface wave signals existed at depth (Figure 4). The velocity-based outliers in panel (a) indicate that the pressure estimates are more reliable, and that the Vector velocities were sometimes noisy.

[28] The likely primary cause of the noise in the Vector-measured velocities is biofouling of the transducer surfaces. Time series of run-mean signal amplitudes, pulse-pair correlation amplitudes, and the percentage of correlation amplitudes exceeding 0.7 indicate that the times of increased scatter in the velocity-based estimates of  $\tilde{u}_b$  from the Vector coincided with times of low pulse-pair correlation magnitudes, and that these lower correlations coincided with low signal amplitudes. On YD289, after the divers had scraped barnacle growth off the transducer surfaces, pronounced increases occurred in the run-mean amplitudes (from 60 to 80), in the run-mean correlations (from 0.5 to 0.9), and in the percent correlations greater than 0.7 (from near 0% to near 100%). For the remainder of the record, the correlations and amplitudes remained generally high, with an association between higher signal amplitudes and times when 100% of the correlations were above 0.7. Some of these times coincided with higher waves and/or mean currents, but not all. There was also a trend toward lower average correlations after YD290. Over the same period, the

water clarity also gradually improved, and since the divers undertook cleaning missions every few days, the suggestion is that this trend was due to lower concentrations of fine-grained particulate material in the water.

[29] Summarizing, like the currents, near-bed wave orbital velocities were relatively weak, with typical maximum values of 6 cm/s rms, and thus maximum significant velocities of 12 cm/s. A typical value of  $T_p$  was 6 s. Wave directions were variable, mainly out of the SW and SE quadrants. The scatter in the Vector-measured  $\tilde{u}_b$  values in Figure 6a on YD287-288 was due to barnacles on the transducers, while later in the record after the barnacles had been removed, the scatter on YD299-301 and on YD303-305 was likely associated with higher water clarity.

### 3.3. Near-Bed Turbulence and Dissipation

[30] Two representative near-bed vertical velocity spectra,  $S_{wvs}$  are presented in Figure 7. Both spectra are from the wave event on YD293-296, one near the peak in the wave forcing, the other later in the event when wave energy was much reduced. The spectra represent averages over the 17 range bins between 1.4 and 12.6 cm above bottom for CDP1. Both spectra exhibit a peak at a frequency of 0.17 Hz, corresponding to the 6-s wave period (Figure 5). Recalling that the CDPs were tilted at  $5^\circ$ , and the frame itself was tilted with respect to the vertical, these “apparent” vertical velocities in the sea-and-swell band include contributions from horizontal wave motions, in addition to true vertical velocities induced by the flow over ripples on the seabed. At frequencies above the gravity wave peak (i.e., above 0.3 Hz), both spectra exhibit slopes close to the  $-5/3$  value characteristic of locally isotropic inertial subrange turbulence, and then a relatively flat noise floor.

[31] The near-bed turbulence intensity was determined as follows. The noise floor was taken to be the minimum value of  $S_{ww}$  above 5 Hz. (The noise floor estimate is discussed further in section 6.3.) After subtracting this noise level, a linear least squares fit of  $\log S_{ww}$  to  $\log f$  was made over the

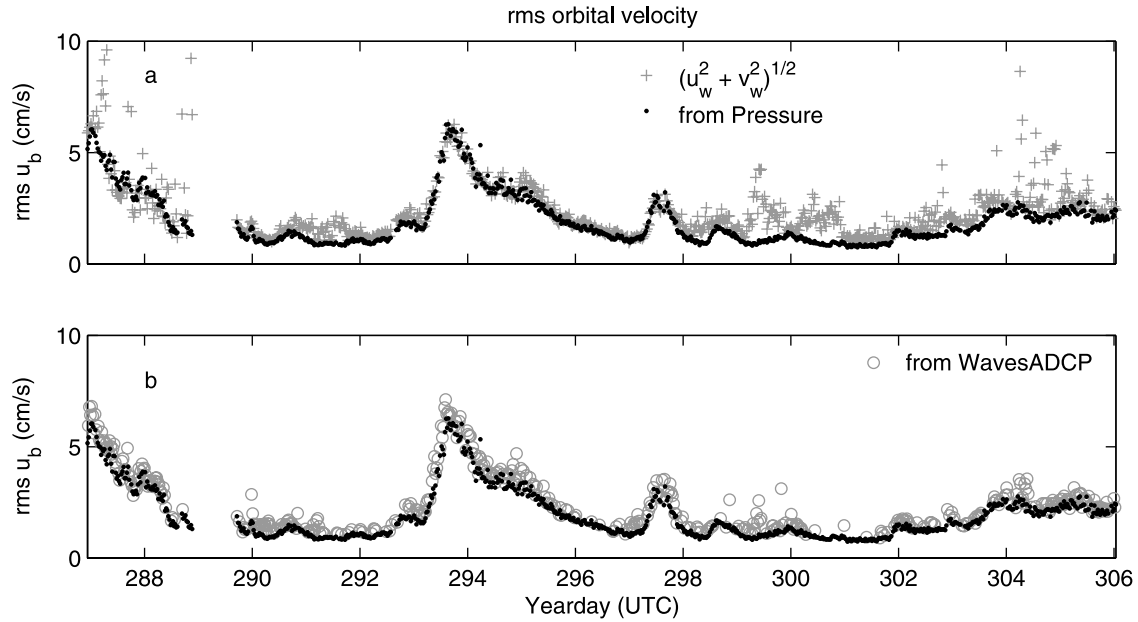


**Figure 6.** (a) Time series of RMS near-bed orbital velocity,  $\tilde{u}_b$ , determined from the Vector data via the square-root of the sum of the  $u$  and  $v$  variances (grey plus), and via the RMS pressure converted to velocity using  $T_p$  and linear theory (solid circle). (b)  $\tilde{u}_b$  determined from the ADCP (grey open circle) based on the variance of the ADCP velocity spectrum in the wind-wave band, likewise converted to RMS near-bed velocity using linear theory (see text). The solid points are the same as in Figure 6a.

interval  $0.3 < f < 1$  Hz. Expressing the resulting fit as a power law, viz.

$$S_{ww} = A_{ww} f^\zeta \quad (8)$$

the variance of the turbulence,  $\sigma_w^2$ , was then determined by integrating the fit between 0.1 and 10 Hz to include contributions to the total turbulence intensity from those parts of the inertial subrange beyond the fitted frequencies: i.e., from within the wind-wave band, 0.1 to 0.3 Hz, where wave-orbital motions mask the turbulence; and from frequencies above 1 to 5 Hz where, depending on wave energy, the turbulence signal is swamped by noise.

[32] Focusing on the interval YD293.5–295.0 when  $\tilde{u}_b$  exceeded 2.5 cm/s, and when the mean flow was westward and CDP1 thus on the upstream side of the frame, the fits to equation (8) yielded  $\zeta = -1.16 \pm 0.24$  (mean  $\pm$  standard deviation), and  $\sigma_w = 0.22 \pm 0.06$  cm/s. Thus  $|\zeta|$  was less than  $5/3$  on average. *Smyth and Hay* [2003] also found that inertial subrange spectral slopes were less steep than  $-5/3$  for near-bed vertical velocity spectra in the nearshore zone, and suggested that the reduced slope likely indicated anisotropy of the near-bed turbulence. While the present results also indicate  $|\zeta| < 5/3$ , the observable width of the inertial subrange was often much less than a decade

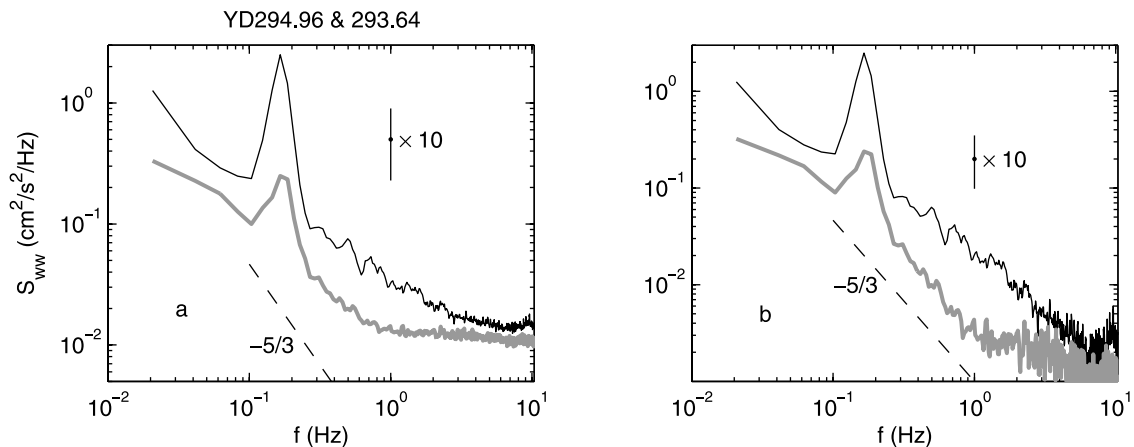


**Figure 7.** Vertical velocity spectra,  $S_{ww}$ , averaged in the vertical over 17 range bins from 1.4 to 12.6 cm above bottom. The error bars represent the 95% confidence interval, shown at  $10\times$  actual size. Data from CDP1, on Yearday 293.64 (black) and 294.96 (grey). Noise levels of 0.012 and 0.01  $\text{cm}^2\text{s}^{-2}/\text{Hz}$  have been subtracted from the spectra in (a) to obtain those in (b). Dashed lines are  $f^{-5/3}$ , as indicated.

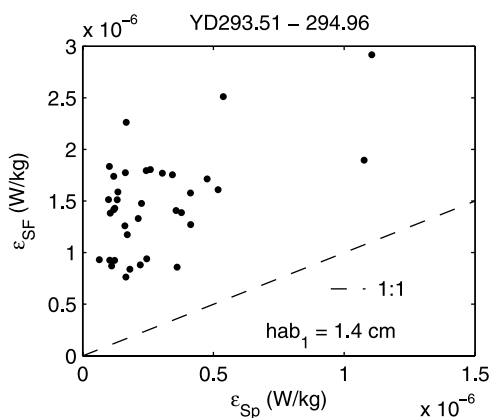


**Figure 8.** Dissipation in the layer 1.4 to 12.6 cm above bottom, determined from the CDP1 vertical velocities. Values are from the structure function method,  $\epsilon_{SF}$ , and the spectral method,  $\epsilon_{Sp}$ . The dashed line is the 1:1 line. Height above bottom of the first bin used in the analysis,  $hab_1$ , is 1.4 cm as indicated.

(Figure 7). Thus these results are consistent with, but do not necessarily imply, anisotropy.

[33] Dissipation rates are plotted in Figures 8 and 9. The spectral estimates,  $\epsilon_{Sp}$ , were obtained using equation (5) evaluated at  $f = 1$  Hz, and thus with  $S_{ww}$  replaced by  $A_{ww}$  from the log-log fits. On the basis of the results obtained by Lumley and Terray [1983], Trowbridge and Elgar [2001], and Bryan *et al.* [2003] for the spectrum of locally isotropic inertial subrange turbulence under waves (see Appendix),  $U$  was set equal to the RMS wave orbital velocity  $\tilde{u}_b$ , and  $B_w$  to 10. The structure function method estimates,  $\epsilon_{SF}$ , were obtained using equation (7) evaluated at 5 different  $\Delta z$  spacings (see below). The values of both  $\epsilon_{Sp}$  and  $\epsilon_{SF}$  represent ensemble averages over the 1.4- to 12.6-cm height interval ( $\epsilon_{SF}$  values were also determined for heights between 0.7 and 12.6 cm, see below). While the two sets of estimates are roughly proportional and roughly coherent, the  $\epsilon_{SF}$  values are offset from  $\epsilon_{Sp}$  by about  $1.5 \times 10^{-6}$  W/kg on average.

[34] Before proceeding farther, the applicability of inertial subrange arguments to these data is examined. The  $\epsilon_{Sp}$  estimates range from ca.  $0.1$  to  $1.1 \times 10^{-6}$  W/kg (Figure 8). The corresponding range of the Kolmogorov microscale,  $\eta_K = (\nu^3/\epsilon)^{1/4}$ , is 1.6 to 0.9 mm (with  $\nu$ , the kinematic viscosity of

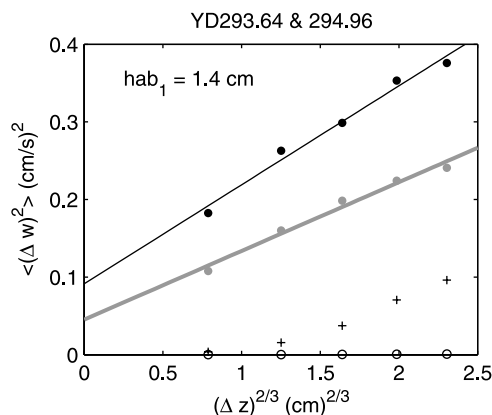


**Figure 10.** Structure function fits. Points indicate the observed values of  $\langle(\Delta w)^2\rangle$  at the 5 different vertical separations. Lines represent the least squares fits. As in Figure 7, runs on Yearday 293.64 and 294.96 are indicated by black and grey respectively. Mean square errors,  $E^2$ , for these two fits are 0.77 and 0.59%. The + and o symbols represent the theoretical maximum possible contributions to  $\langle(\Delta w)^2\rangle$  from potential flow over sinusoidal ripples. See section 6.2 for details.

water, equal to  $0.89 \times 10^{-2}$  cm<sup>2</sup>/s at 25°C). This microscale range is much less than the 7-mm spacing between CDP range bins, and the higher  $\epsilon_{SF}$  values would yield still smaller estimates of  $\eta_K$ . Thus the structure function method (equation (6)) should be sufficiently valid to provide a first-order estimate of  $\epsilon$ . The value of  $\eta_K$  can be used to estimate the high-frequency limit of the inertial subrange. With  $k_K \eta_K = 0.2$  at the peak of the dissipation spectrum [Tennekes and Lumley, 1972, p. 271], and using  $\tilde{u}_b$  with Taylor's hypothesis as before,  $f_K = 1.0$  to 2.3 Hz for  $\epsilon$  ranging from  $0.1 \times 10^{-6}$  to  $3 \times 10^{-6}$  W/kg. Thus by using 10 Hz as the upper limit of integration in the spectral method, the values of  $\epsilon_{Sp}$  have been slightly overestimated: for a  $-5/3$  spectrum, by about 9% at  $\epsilon = 0.1 \times 10^{-6}$  and by about 4% at  $3 \times 10^{-6}$  W/kg. Given the scatter in the data, these differences are small.

[35] Returning to Figure 8, the values of  $\epsilon_{SF}$  were determined from velocity differences at non-overlapping spacings of 1, 2, 3, 4, and 5 bins (0.7 to 3.5 cm), and a linear least squares fit of  $\langle(\Delta w)^2\rangle$  to  $(\Delta z)^{2/3}$  in the  $z$ -interval 1.4 to 12.6 cm above bottom. With  $m$  being the best fit slope

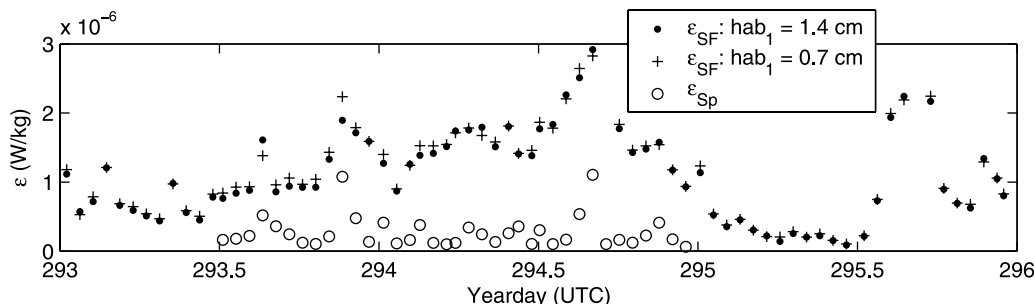


**Figure 9.** Dissipation time series. Values of  $\epsilon_{SF}$  are shown for two minimum heights above bottom, 0.7 and 1.4 cm.

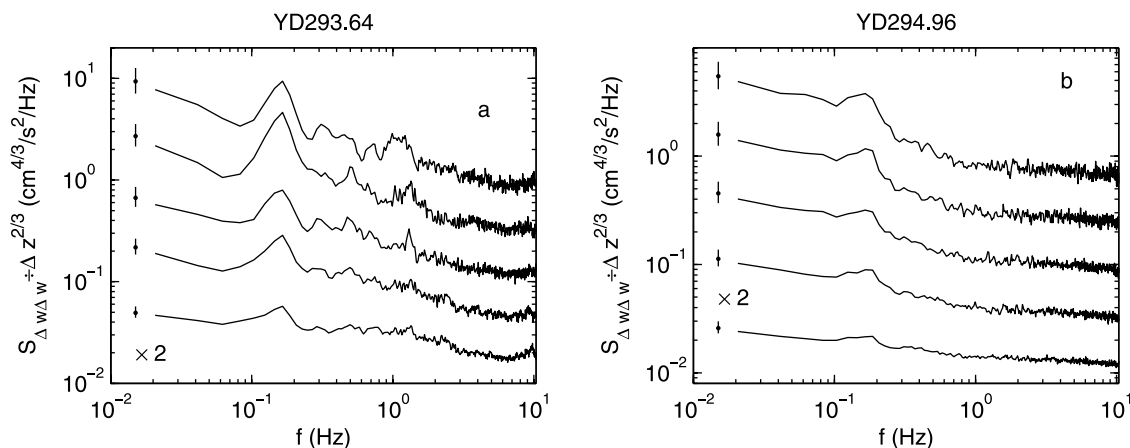


**Figure 11.** Spectra of vertical velocity differences for the 5 different  $\Delta z$  values used in the structure function fits. Note the scaling of  $S_{\Delta w \Delta w}$  by  $\Delta z^{2/3}$  (see equation (6)). Successive spectra are offset by a factor of 2. Error bars indicate 95% confidence intervals, shown at  $2\times$  actual size.

and using equation (7),  $\epsilon_{SF}$  is then given by  $[m/C]^{3/2}$ . A mean square error for the fits was defined as

$$E^2 = \sum_{i=1}^4 \frac{(y_i - \hat{y}_i)^2}{\hat{y}_i^2} \quad (9)$$

where  $y_i$  and  $\hat{y}_i$  respectively represent the observed and best fit values at the  $i$ th spacing.  $E^2$  was less than 1.5% (0.72% mean, 1.29% maximum) over the time spanned by the data in Figure 9. The fits for the two representative runs are shown in Figure 10. The  $y$ -intercept is the noise variance in equation (7). The mean value of  $\sigma_n$  obtained from the fits was  $0.23 \text{ cm/s} \pm 0.05 \text{ cm/s}$  standard deviation.

[36] The spectra of  $\Delta w$  for the two representative runs are shown in Figure 11 for each of the 5 spacings. Compared to  $S_{ww}$  (Figure 7), the 6-s period wave peak has been significantly suppressed, by a factor of 2 or more. This energy suppression in the wind-wave band is expected, since the vertical shear and vertical strain rate of the wave orbital motions should be small at these length scales, provided the measurements are well outside the wave bottom boundary layer and the ripple steepness is small (see section 6.2). Regardless of its origin, these spectra indicate that the residual peak, together with the spectral reddening at lower frequencies, represent the likely explanation for  $\epsilon_{SF}$  being almost an order of magnitude larger than  $\epsilon_{Sp}$ . Thus it is assumed for now that the higher values of  $\epsilon$  obtained from the structure function method are real, and due to turbulence from low-frequency motions such as mean currents and internal waves, and to wave-induced turbulence not accounted for in the spectral method (with the caveat that the vertical strain rate and shear due to the ripple-induced perturbation to the interior potential flow may not be small, section 6.2).

## 4. Results II: Bed Forms

### 4.1. Fanbeam and Video Imagery

[37] A rotary fanbeam image acquired upon reconnection to Dalpod1 after the passage of Tropical Storm Matthew is shown in Figure 12. Well-defined long-crested ripples with

ca. 50-cm wavelengths are present throughout the 10-m diameter area imaged by the sonar. The ripple crests are oriented such that the normal to the crests is roughly  $20^\circ$  counterclockwise from shorenormal, consistent with the ca.  $160^\circ$  True wave directions registered by NDBC buoy 42039 during TS Matthew. Figure 13a is a 2.5-m  $\times$  4-m subarea from the offshore side of the full image in Figure 12. This same area as it appeared in the sonar images 15 days later is shown in Figure 13b. Note the pronounced alteration in the appearance of the 50-cm wavelength ripples, especially the reduced extent of the acoustic shadows on the offshore side of the ripple crests, indicating a marked reduction in crest height. Note also the small-scale texture more or less evenly distributed over the surface in the later image. This texture is largely due to small pits in the sediment surface. Pits are also present in the initial image (Figure 14), but in much smaller numbers.

[38] The pits are biological in origin, and were generated mainly by fish. Figure 15 is a sequence of 3 video frames of a pit being created by a triggerfish, presumably feeding on an organism in the seabed. Not all fish-seabed interactions leading to pit formation were associated with feeding activity. Other interactions involved rapid body undulations with the underbelly of the fish next to the seabed to excavate a pit, much like spawning salmon in gravel bedded rivers. Other fish-seabed interactions not leading to pit formation but contributing to the redistribution of bed sediments were observed: for example, fish scraping their sides against the bottom.

### 4.2. Bed Elevation Profiles and Elevation Spectra

[39] The time sequence of bed elevation profiles obtained with the rotary pencilbeam sonar is shown in Figure 16. Each plotted profile represents the ensemble average of 12-h of data. The ripple crests diminish over time, and there is a marked reduction in the skewness of the bed profiles (i.e., crests become less peaked, troughs less broad) early in the profile sequence.

[40] Bed elevation spectra,  $S_{\eta\eta}$ , were computed from the elevation profiles and are plotted in waterfall form in Figure 17. The primary ripple peak at 2 cpm, corresponding

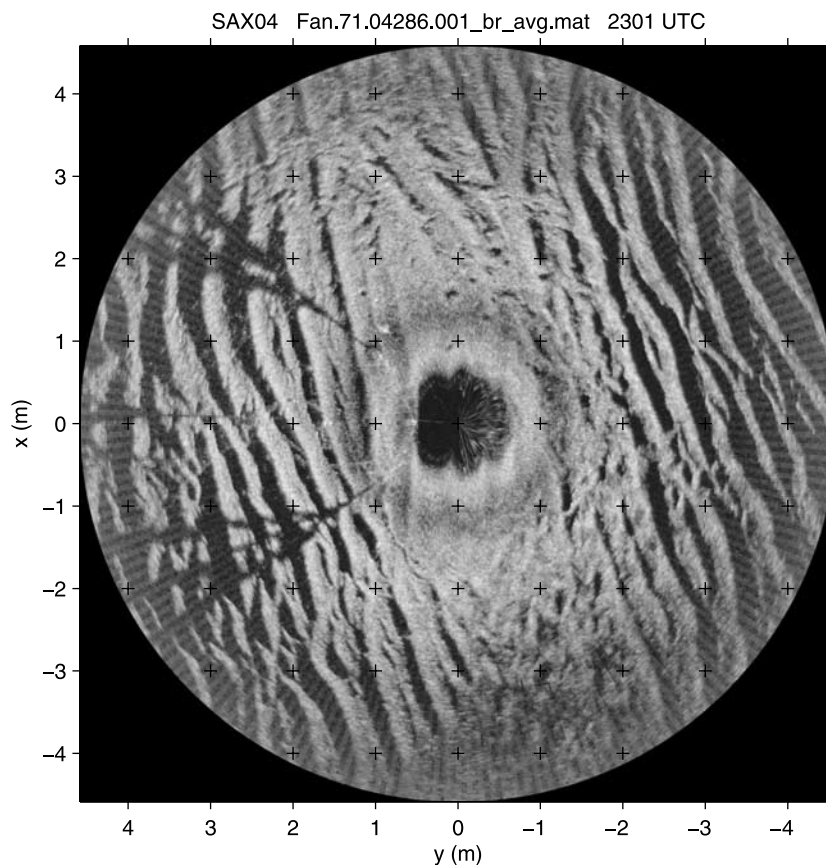


**Figure 12.** Rotary fanbeam image of the seabed on YD286 at 2301 h UTC. Alongshore coordinate ( $x$ ) is +ve eastward; cross-shore coordinate ( $y$ ) is +ve shoreward. Grid marks (plus) are at 1-m intervals. Lighter shades of grey indicate higher signal amplitudes. Note the ca. 50-cm wavelength ripples.

to the ca. 50-cm wavelength ripples in Figure 12, gradually decayed over the 15-d period from YD288 to YD303.

[41] Daily ensemble-averages of  $S_{\eta\eta}$  are plotted in Figure 18 on a logarithmic scale to examine the behavior of the spectra at high spatial frequencies. As indicated in the Figure, a power law fit to the spectra (i.e.,  $S_{\eta\eta} = A_{\eta\eta} f^{\zeta}$ ) was carried out for spatial frequencies from 8 to 24 cpm. Time series of  $\sigma_{\eta}$ , with  $\sigma_{\eta}^2$  representing the variance, are shown in Figure 19a. Three sets of points are plotted: the values of  $\sigma_{\eta}$  from each bed elevation profile (grey dots); the values from the 24-h ensemble-averaged spectra in the 1–3 cpm band corresponding to the primary ripple peak (solid dots); and those for the high-frequency 8–24 cpm band ( $x$ ), also computed from the 24-h ensemble-averaged spectra. The peak RMS amplitude of the primary ripple band drops to 70% of its initial value in about 8 days: this represents the timescale for ripple decay to 50% of the initial variance. Note that in contrast to the  $O(1)$  temporal variation in  $\sigma_{\eta}$  for the primary ripple band, including the steady decline during the first 15 days of the record, the RMS amplitude at high spatial frequencies remained essentially constant throughout the 19-d period. The values of  $\zeta$  obtained from the fits are shown in Figure 19b, and range from about  $-2$  to  $-3$ , with a mean of  $-2.4$ . The error bars indicate the 95% confidence intervals for the estimates, reduced by a factor of 4 to fit on the graph. Consequently, the temporal variations in  $\zeta$  are

small relative to the probable error in the slopes obtained from the log-log fits, and  $\zeta$  can be taken to be constant. Thus these results indicate that the process of ripple degradation was accompanied by an equilibrium spectrum at high spatial frequencies, suggesting a balance between the production and dissipation of bed elevation fluctuations at small spatial scales.

## 5. Results III: Bottom Friction

### 5.1. Stress Estimates

[42] The friction velocity,  $u_*$ , is related to dissipation through  $\epsilon \sim u_*^3/L$ , where  $L$  is a length scale corresponding to the largest eddies or, equivalently, to the turbulence production scale [Tennekes and Lumley, 1972, p. 68 and p. 271]. Associating the latter with the peak in the structure function spectra at the wind-wave frequency, and therefore with turbulence produced by wave orbital motion over the ripples, one possible choice for  $L$  is the ripple height,  $\eta_R$ . From Figure 19a,  $\sigma_{\eta} \sim 1.3$  cm on YD293–295. With  $\eta_R = 2\sqrt{2}\sigma_{\eta}$  for sinusoidal ripples,  $\eta_R = 3.4$  cm. With  $L = \eta_R$ , and  $\epsilon = 1.1 \times 10^{-6}$  to  $3 \times 10^{-6}$  W/kg (the maximum values of  $\epsilon_{Sp}$  and  $\epsilon_{SF}$ , section 3.3), the probable range of maximum values of  $u_*$  indicated by the dissipation estimates is 0.33 to 0.47 cm/s.

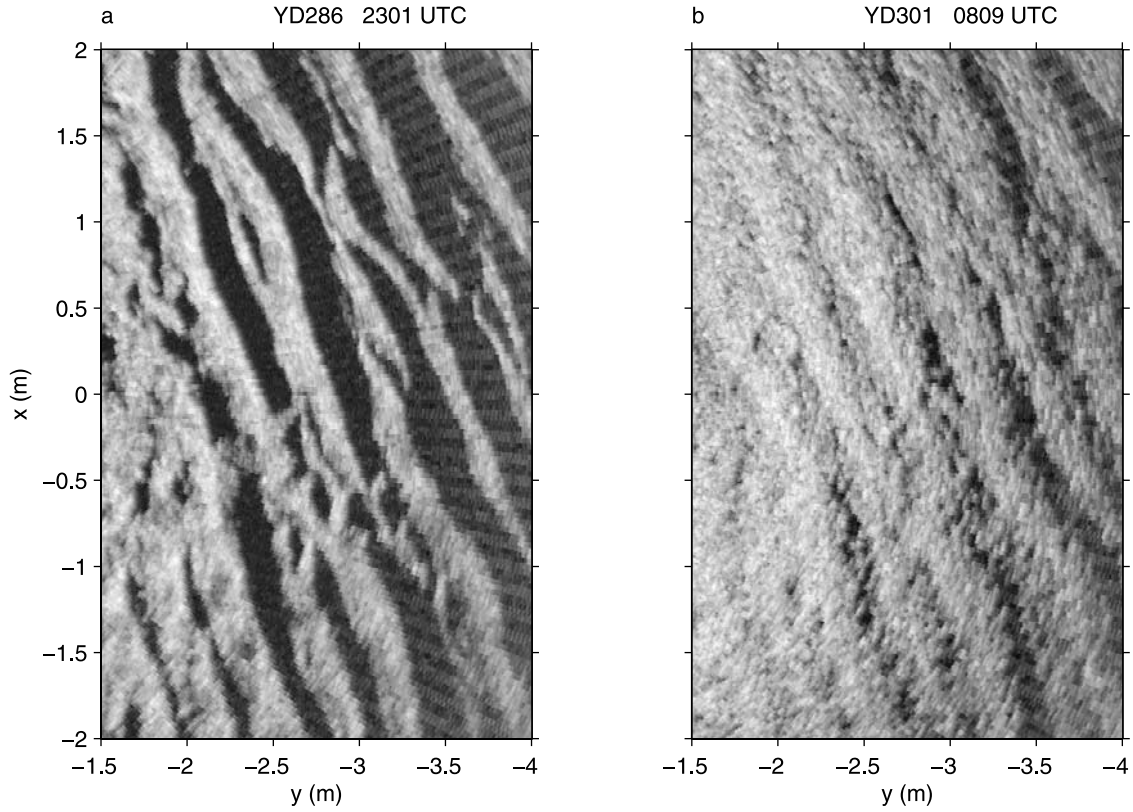


**Figure 13.** Subareas from the offshore side of two fanbeam images: (a) from the image in Figure 12 immediately following Tropical Storm Matthew; and (b) the same area 15 days later. Note the degradation of the ca. 50-cm wavelength ripples.

[43] The friction velocity can also be estimated from the RMS vertical turbulent velocity [see *Smyth and Hay, 2002*, and references therein] via the relation

$$u_* = 2\sigma_w. \quad (10)$$

[44] With  $\sigma_w = 0.22 \pm 0.06$  cm/s (section 3.3), this relation gives  $u_* = 0.44 \pm 0.06$  cm/s, which overlaps the range of maximum values obtained from the dissipation estimates.

[45] The Shields parameter, or non-dimensionalized shear stress [see, e.g., *Nielsen, 1992*, p. 104], is given by

$$\theta = \frac{\tau_o/\rho}{(s-1)gD_{50}}, \quad (11)$$

where  $s$  is the specific gravity of the sediment grains,  $g$  is the gravitational acceleration, and

$$\tau_o/\rho = u_*^2, \quad (12)$$

$\tau_o$  being the peak stress during the wave cycle, and  $\rho$  the fluid density. With  $D_{50} = 405 \mu\text{m}$  and the above range of values for  $u_*$ ,  $0.002 < \theta < 0.003$ . These values are more than an order of magnitude below  $\theta_c \sim 0.05$ , the value at the threshold for sediment motion.

[46] Finally, the wave friction factor can be estimated from

$$\frac{\tau_o}{\rho} = \frac{f_w}{2} u_{bo}^2. \quad (13)$$

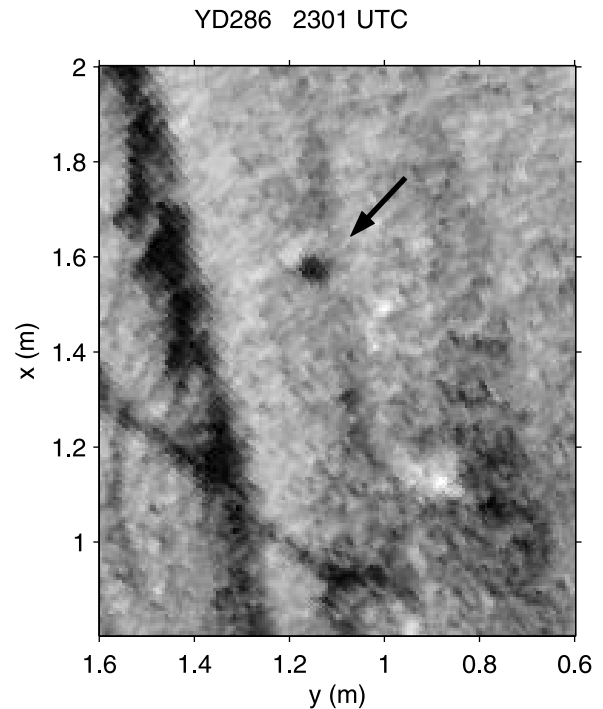


**Figure 14.** Subarea from the image in Figure 12. A ca. 10-cm diameter pit in the seabed is indicated by the arrow.

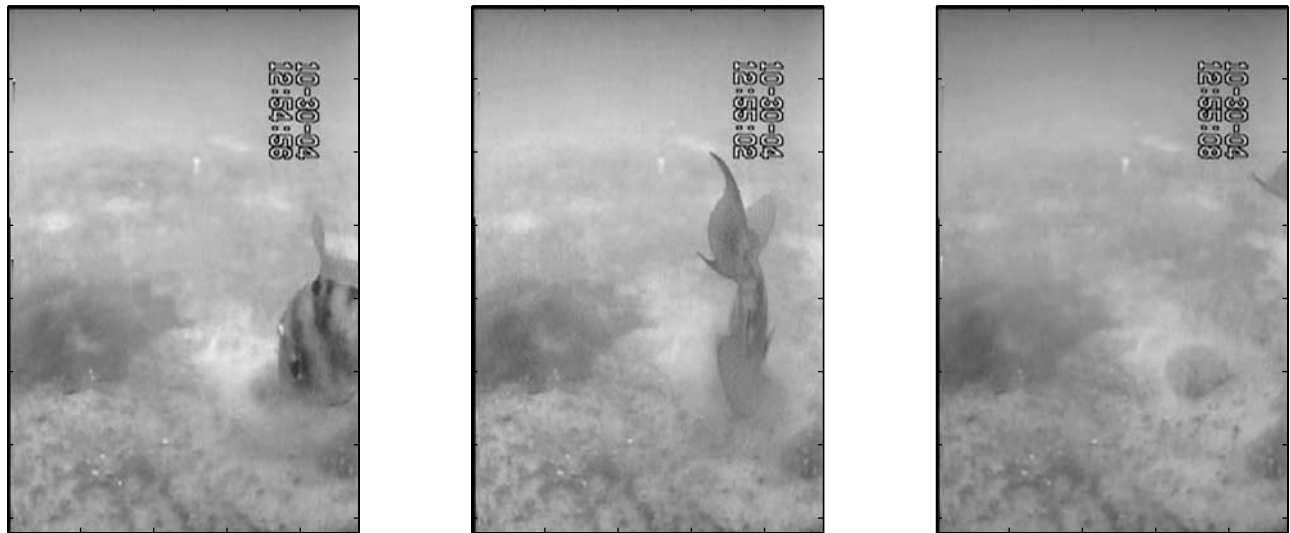


**Figure 15.** Video frames showing a triggerfish making a pit in the seafloor on 30 October 2004 (YD304). The frames are 6-s apart, as indicated by the time code on the upper right in each panel.

[47] For  $u_* = 0.3$  to  $0.5$  cm/s, and  $\tilde{u}_{bo} = 5$  cm/s,  $f_w$  would range from  $0.9 \times 10^{-2}$  to  $2.0 \times 10^{-2}$ , a reasonable range of values given the degraded state of the ripples (see next section). The friction velocity under the significant wave (the average of highest-1/3 waves) would be  $u_{*1/3} = \sqrt{f_w/2}u_{b1/3}$ .

Setting  $u_{b1/3} = 2\tilde{u}_b$  [Thornton and Guza, 1983], these  $f_w$  values give  $u_{*1/3} \sim 0.67$  to  $0.93$  cm/s and hence  $\theta_{1/3} \sim 0.007$  to  $0.013$  for  $D = 405 \mu\text{m}$ , which is still much less than  $\theta_c$ .

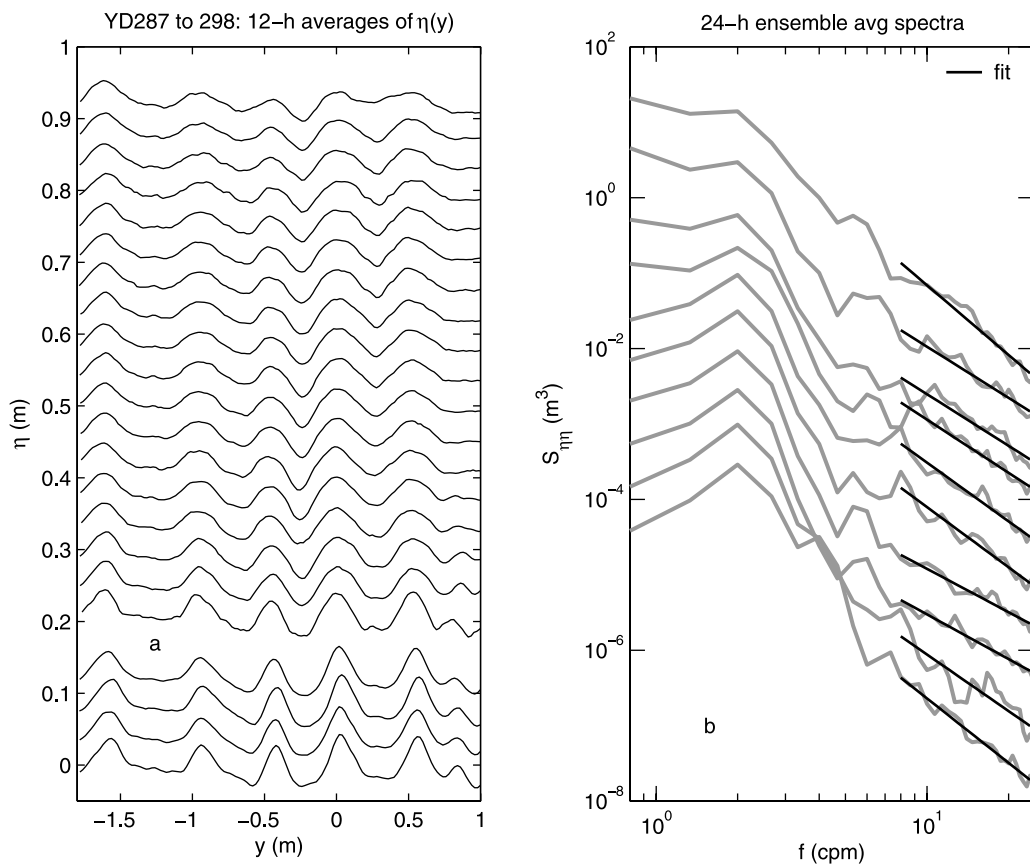


**Figure 16.** Bed elevation profiles on the offshore side of the instrument frame, from the rotary pencilbeam sonar for YD287 to 298. The profiles have been ensemble-averaged over 12-h intervals. The vertical spacing is proportional to time, and time increases from bottom to top.

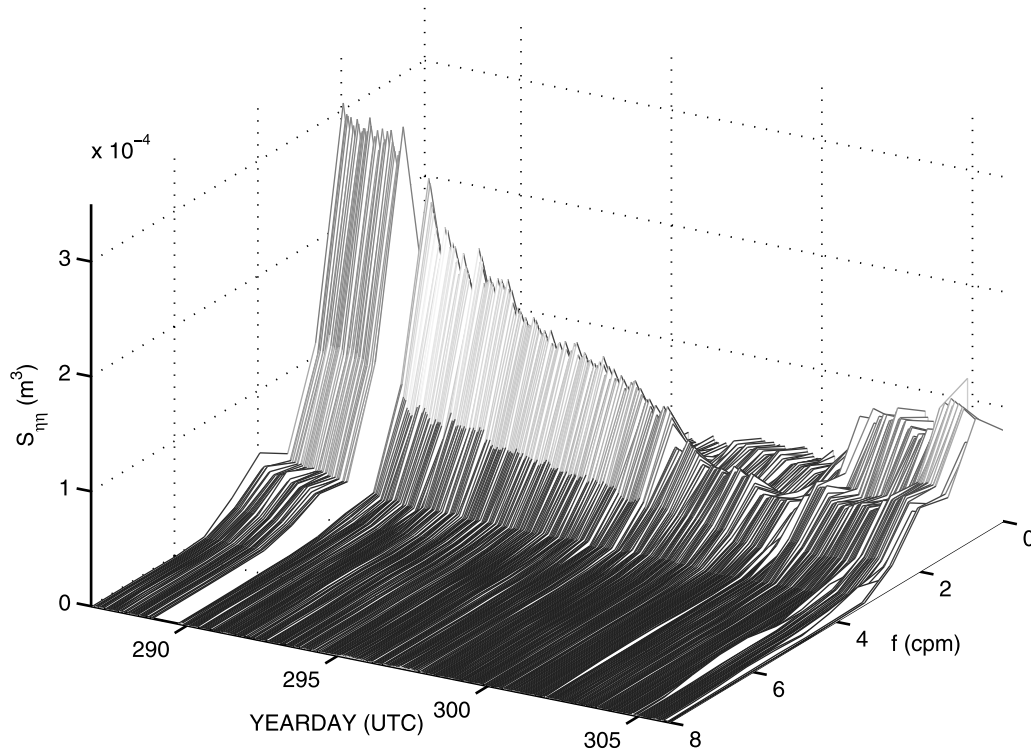


**Figure 17.** Waterfall plot of bed elevation spectra,  $S_{\eta\eta}$ . Note the decay of the primary peak at 2 cpm over the first 15 days.

[48] Thus these results indicate that the peak shear stress at the bed remained below  $\theta_c$  for both the maximum average wave and for the maximum significant wave during the period in question. Consequently, sand grain movement due to fluid motion would be expected to have occurred only occasionally, in response to the highest waves and to peak fluctuations in the near-bed turbulence.

## 5.2. Wave Friction Factors

[49] Figure 20 is a plot of the wave friction factor  $f_w$  versus normalized Shields parameter,  $\theta_D/\theta_c$ . The solid grey and dashed grey curves are predictions made using semi-empirical formulae both for fixed-grain roughness flat beds and for mobile sediment beds.

[50] The ordinates for the fixed-grain roughness (dashed grey) curve were computed for 6-s period waves using the formula suggested by Swart [1974] based on the work of Jonsson [1966] [see also Nielsen, 1992]:

$$f_w = \exp[5.213(r/A)^{0.194} - 5.977], \quad (14)$$

where  $A = \tilde{u}_o/\omega$  is the wave-orbital semi-excursion in the interior (i.e., outside the wave bottom boundary layer). The values of  $f_w$  along the dashed grey curve were computed with the roughness  $r$  set equal to  $D_{50} = 405 \mu\text{m}$ : thus, these values are denoted  $f_{wD}$ . The abscissa in this figure represents the fixed-grain Shields parameter computed using  $f_{wD}$  in equation (11), and so are denoted by  $\theta_D$ .

[51] Nielsen [1992] has suggested an alternate form for equation (14), based in part on more recent data than were available to Swart: viz.

$$f_w = \exp[5.5(r/A)^{0.2} - 6.3]. \quad (15)$$

The thin dashed black line in Figure 20 was computed using equation (15) with  $r = D_{50}$ .

[52] The ordinates for the mobile bed curve (solid grey) were obtained for 8-s period waves, corresponding to the likely wave period during ripple formation (see below), using the relations suggested by Tolman [1994]. His relations are based on the results of Madsen *et al.* [1990] for relative roughness due to sand ripples formed under irregular waves, on the sheet flow roughness expression suggested by Wilson [1989], and on the analytic solution for the vertical structure of the wave bottom boundary layer obtained by Grant and Madsen [1982] assuming a time-independent eddy viscosity. The theoretical expressions for the friction factor are

$$f_w = 2\kappa^2 \zeta_o \frac{\ker_1^2 2\sqrt{\zeta_o} + \text{kei}_1^2 2\sqrt{\zeta_o}}{\ker^2 2\sqrt{\zeta_o} + \text{kei}^2 2\sqrt{\zeta_o}}, \quad (16)$$

and

$$\frac{k_N}{2A} = 21.2\kappa\sqrt{f_w}\zeta_o, \quad (17)$$

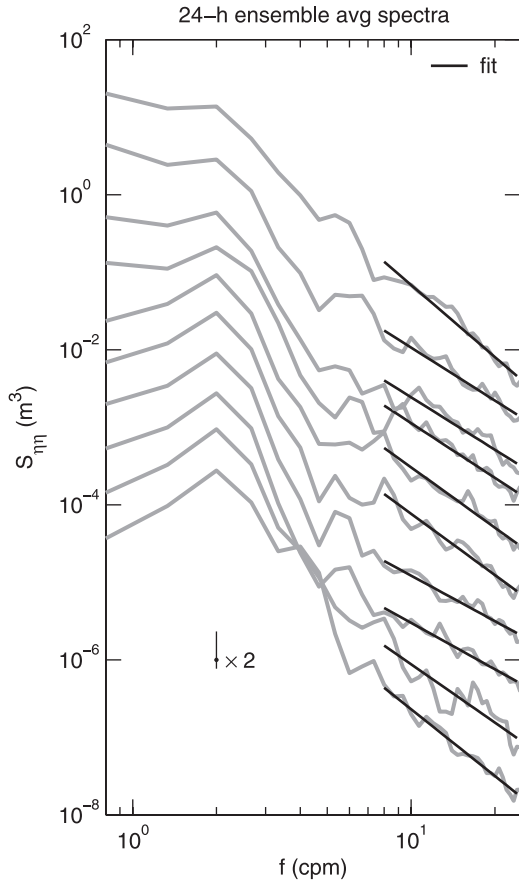


**Figure 18.** Log-log plot of bed elevation spectra showing the power law behavior of  $S_{\eta\eta}$  at high spatial frequencies. Solid black lines indicate the power law fit. Individual spectra represent ensemble averages of  $S_{\eta\eta}$  over 24-h intervals. Time increases from bottom to top. Successive spectra are offset by a factor of 2. The error bar represents the 95% confidence interval, shown at  $2\times$  actual size.

where  $k_N/2A$  is the relative roughness,  $\kappa = 0.4$  is von Karman’s constant,  $\ker$  and  $\kei$  are Kelvin functions,  $k_N$  is the Nikuradse equivalent roughness of the bed,  $\zeta_o = \omega z_o/\kappa u_*$ , and the flow is assumed to be rough turbulent (i.e.,  $z_o = k_N/30$ ). (Note that  $k_N$  and  $r$  are equivalent.) *Grant and Madsen* [1982] and *Tolman* [1994] use an approximate form of equation (16), valid for  $\zeta_o \ll 1$ . Given a value for the relative roughness, equations (16) and (17) can be solved for  $f_w$ . Since the interest here is in low to moderate energy conditions, the sheet flow contribution to the total roughness is not relevant. The ripple roughness predictor suggested by *Madsen et al.* [1990] for irregular wave conditions is

$$k_N = 1.5A \left( \frac{\theta'_D}{\theta_c} \right)^{-2.5}, \quad (18)$$

where  $A$  and  $\theta'_D$  are based on the RMS wave orbital velocity,  $\tilde{u}_b$ .  $\theta'_D$  is also based on  $f'_{wD}$ , computed using the wave bottom boundary layer (WBBL) solution (i.e., equations (16) and (17)) with  $k_N = D_{50}$ . Over the parameter range of interest here, the values of  $\theta'_D$  and  $\theta_D$  differ by only a few percent (see below).

[53] The solid dots in Figure 20 are based on the CDP results (see the previous section), with  $f_w$  computed from equations (12) and (13)  $u_* = 0.3$  and  $0.5$  cm/s and  $\tilde{u}_b = 5$  cm/s. Two sets of data points are shown, each set corresponding to a different value of the abscissa. For the solid grey dots,  $f_{wD}$  was computed using equation (14), while the solid black points ( $\bullet$ ) are based on equation (15), using  $T_p = 6$  s and  $\tilde{u}_b = 5$  cm/s in both cases.

[54] For natural sands, it is common to take  $r > D_{50}$  [*Kamphuis, 1975; Sleath, 1984; Nielsen, 1992*]. In Figure 21, results similar to those in Figure 20 are presented but with the fixed-grain values  $f_{w2.5}$  and  $\theta_{2.5}$  computed using equation (15) with  $r = 2.5D_{50}$ . The values for  $f_w$  for the

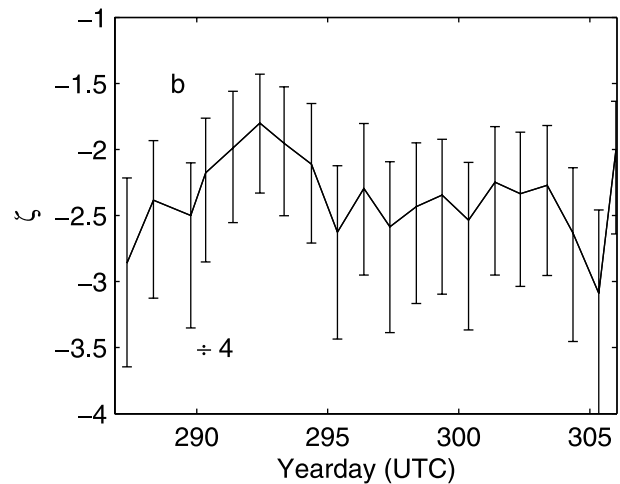
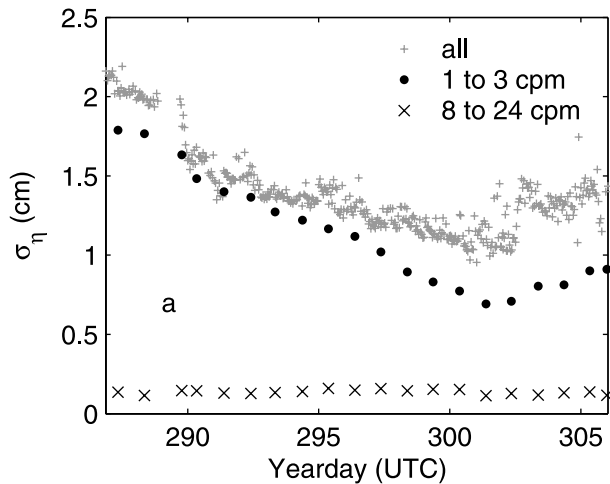


**Figure 19.** (a) Time series of RMS bed roughnesses,  $\sigma_{\eta}$  from the bed elevation profiles. Grey dots indicate the variance from the detrended individual elevation profiles. Solid black dots represent the square-root of the variance in the 1 to 3 cpm band (i.e., the spatial frequency band corresponding to the ca. 50-cm wavelength primary ripples) from the 24-h ensemble-averaged elevation spectra. Black  $\times$ s similarly indicate the square-root of the variance in the high spatial frequency band, 8 to 24 cpm. (b) The exponents from the power law fit to  $S_{\eta\eta}$  in the 8 to 24 cpm spatial frequency band. Error bars indicate the 95% confidence intervals, shown at  $4\times$  smaller than actual size.

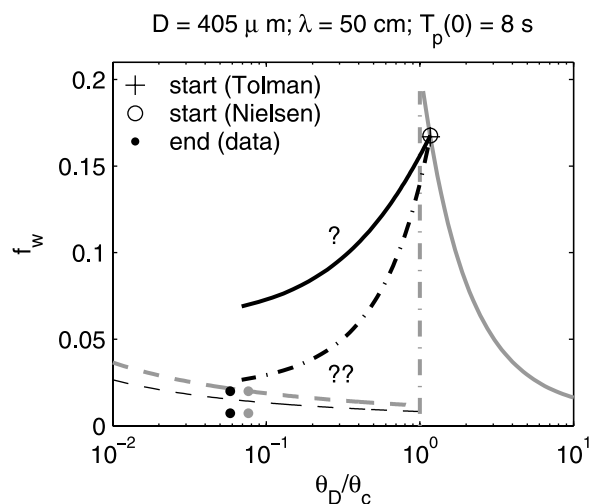


**Figure 20.** Wave friction factor,  $f_w$ , versus Shields parameter ratio,  $\theta_D/\theta_c$ , for 405- $\mu\text{m}$  diameter sand. The solid grey curve is the prediction based on Tolman [1994] for mobile sediments and 8-s period waves. The vertical dash-dot line indicates the threshold of grain motion. The dashed grey curve to the left of the critical Shields parameter (i.e., below the threshold of grain motion) is based on equation (14) for fixed sediment grains on a flat surface, with  $r = D$ . The dashed black curve also represents  $f_w$  for fixed-grain roughness, but is based on equation (15). The solid black points are the measured values of  $f_w$  at roughly the midpoint of the ripple decay record (section 5), plotted at  $\theta_D$  computed using equation (15). The solid grey points also represent the data, but with  $\theta_D$  computed using equation (14). The open circle and plus indicate the likely equilibrium points for 50-cm wavelength orbital ripples formed during Tropical Storm Matthew, computed as indicated in the text. The solid black and dashed black curves, labeled by interrogation marks, indicate potential  $f_w$  versus  $\theta_D$  trajectories during ripple decay (see text for discussion).

active transport region (solid grey curve) are higher than the corresponding curve in Figure 20 because at a given value of  $\theta_{2.5}$  the smaller value of  $\theta'_D$  leads to an increased relative ripple roughness (equation (18)). Also plotted in Figure 21 is the  $f_w$  curve for a smooth wall, given by

$$f_w = \frac{2}{\sqrt{Re}}, \quad (19)$$

where  $Re$  is the wave Reynolds number given by  $Re = \tilde{u}_{ob}A/\nu = \tilde{u}_{ob}^2/(\nu\omega)$ . This relation is valid for  $Re < 3 \times 10^5$  [Nielsen, 1992, p. 24]. The smooth-wall  $f_w$  values shown in the figure, computed with  $T_p = 6$  s, correspond to  $Re < 1.2 \times 10^5$ . On the basis of a 10-cm/s significant wave orbital velocity (i.e.,  $2\tilde{u}_b$ ),  $10^4$  is a representative upper limit of  $Re$  for the data. The solid grey dots in Figure 21 are the CDP values for  $f_w$  computed using the same range of  $u_*$  values as in Figure 20, but with  $\tilde{u}_{bo} = \sqrt{2} \tilde{u}_b = 7.1$  cm/s. These points fall well below the fixed-grain curve for fully rough turbulent flow, and below the smooth wall curve, and are therefore clearly too small.

[55] The data can be reconciled with the predicted curves if “significant” turbulent and wave orbital velocities are

used to estimate  $u_*$  and  $f_w$ : i.e., analogous to  $\tilde{u}_{1/3} = 2\tilde{u}_b$ , equation (10) is rewritten as  $u_{*1/3} = 2(2\sigma_w)$ , and thus  $f_w = 2[\sigma_w/\tilde{u}_b]^2$ . This approach has been used to estimate  $f_w$  from near-bed turbulence measurements in active transport conditions (i.e., to the right of  $\theta/\theta_c = 1$ ), with promising results [Smyth and Hay, 2002; Trembanis et al., 2004; Newgard and Hay, 2007]. The solid black dots (●) in Figure 21 represent the values of  $f_w$  computed this way with  $\sigma_w = 0.38$  and 5.0 cm/s, and  $\tilde{u}_b = 5$  cm/s. The corresponding values of  $\theta_{2.5}$  were also computed using significant parameter values:  $A_{1/3} = \tilde{u}_{b1/3}/\omega$  in equation (14) (with  $r = 2.5D_{50}$ ). These data points are clearly in much better agreement with the semi-empirical predictions, nearly bracketing both the smooth bed and the rough fixed-grain curves close to the point where the two curves intersect.

### 5.3. Ripple Degradation Trajectories

[56] The CDP data points (●) in Figures 20 and 21 represent a state of the rippled bed at a point along its evolutionary trajectory in  $f_w, \theta$  parameter space. The ●-points thus represent an endpoint from which a trajectory passing through previous states could in principle be traced, given sufficient knowledge and understanding of the system. Alternatively, given a starting point representing the ripples at their time of formation, trajectories could be traced forward in time toward the endpoint. While observations are not available from the time period when Tropical Storm Matthew passed through the area, conditions at the time of formation can be estimated. The question asked here is whether, given a common starting point, existing semi-empirical formulae for ripple roughness etc. are able to predict the observed endpoint. Note that this question is independent of the actual shape of the path.

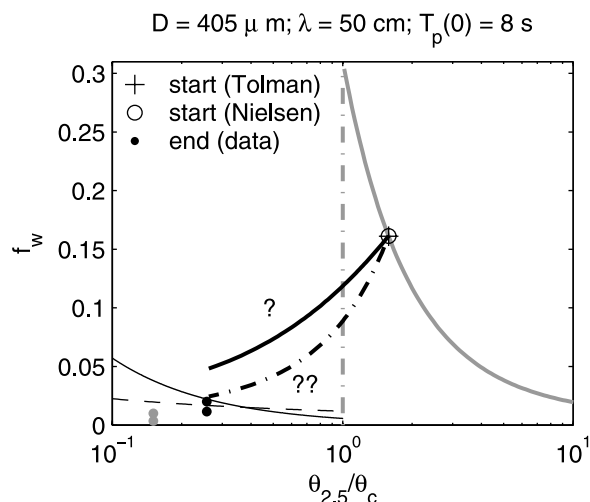


**Figure 21.** Wave friction factor,  $f_w$ , again plotted versus Shields parameter ratio but in this case  $\theta_{2.5}/\theta_c$ , instead of  $\theta_D/\theta_c$  as in Figure 20. Note also the changes in the axis scales. Other differences from Figure 20 are: (1) the thin solid black line, representing the smooth wall result, equation 19 and (2), Swart’s fixed-grain roughness result, equation (14), is not shown. Also, the solid black data points have been computed using the significant turbulence levels and wave orbital velocity (see text).

[57] Assume as the initial condition that the ripples left behind after the passage of TS Matthew were fully developed (i.e., equilibrium) orbital ripples. The wave orbital diameter at this nominal starting point would then be given by the well-known proportionality between wave orbital excursion and orbital ripple wavelength [Clifton and Dingler, 1984; Wiberg and Harris, 1994; Traykovski et al., 1999]:

$$2A \simeq \lambda/0.7, \quad (20)$$

where  $\lambda$  is the ripple wavelength. Using this relation and  $\lambda = 50$  cm to estimate  $A$ , values of the fixed-grain friction factor ( $f_{wD}$  or  $f_{w2.5}$ ) and thus the Shields parameter at the starting point can be computed from equations (14) (or (15)) and 11 for a given wave period. The value of  $T_p$  registered by NDBC buoy 42039 during TS Matthew was 7.7 s. Allowing for a shift to lower frequencies due to the low-pass filter effect of the 17-m water column,  $T_p$  at the starting point is taken to be 8 s. The + symbols in Figures 20 and 21 represent the points on the Tolman curve at the corresponding value of  $\theta_D$  or  $\theta_{2.5}$ .

[58] A second estimate of the starting point can be obtained by using the relation for ripple roughness proposed by Nielsen [1992], viz.

$$r = C_N \eta_R^2 / \lambda, \quad (21)$$

where  $C_N$  is a constant which Nielsen determined to have a value of 8 based on experimental data. For equilibrium orbital ripples,  $\eta_R/\lambda \sim 0.2$  [Nielsen, 1981]. This relation, together with equations (21), (20), and (14) yield the point represented by the open circle in Figures 20 and 21. To obtain close agreement between the two starting point estimates,  $C_N$  was reduced to 5.8 in Figure 20, and to 6.4 in Figure 21. A reduced value of  $C_N$  is consistent with the observation by Madsen et al. [1990] of lower relative roughnesses under irregular waves.

[59] The solid black curve in Figure 20 is one of many possible forward trajectories. This path was computed assuming that  $T_p$ ,  $\tilde{u}_b$  and  $\eta_R$  decreased linearly from their values at the starting point to their values at the endpoint defined by the  $\theta_D$  value of the observations. Nielsen's relation for ripple roughness, equation (21) with  $C_N = 5.8$ , and equation (14) were used to compute  $f_w$  along the path.  $\theta_D$  along the trajectory was computed using equation (14) with  $r = D_{50}$ . There is a large discrepancy between the endpoint of this trajectory and the observed endpoint. The discrepancy can be overcome if  $C_N$  is allowed to decrease as the ripple height degrades. For the black dot-dashed trajectory shown in the figure,  $C_N$  decreased linearly, in step with  $T_p$  to a final value of 1.

[60] A similar set of probable starting points and possible trajectories are shown in Figure 21, but using  $r = 2.5D_{50}$ . The larger grain roughness shifts the starting point on the Tolman curve farther to the right of the threshold of grain motion. The solid black trajectory again corresponds to a fixed value of  $C_N$ , 6.4 in this case. The discrepancy between the observed and computed endpoints is much reduced compared to Figure 20. The dot-dashed black path again corresponds to  $C_N$  decreasing along the path. In this case a

final value of 2.0 was required to obtain close agreement with the observations.

[61] Thus the results in Figures 20 and 21 indicate that using a time-dependent value of  $C_N$  produces better agreement with the observed values of  $f_w$  at the endpoint, suggesting a possible dependence of  $C_N$  on ripple age. In addition, the results indicate that using  $r = 2.5D_{50}$  for the grain roughness reduces the difference between the predicted endpoints for constant and time-varying  $C_N$ .

## 6. Discussion

### 6.1. Dissipation Rates

[62] Turbulent kinetic energy dissipation rates in the vicinity of the seabed and in the presence of waves have been measured previously, mainly close to shore both within and outside the surf zone. George et al. [1994] found rates of  $5 \times 10^{-5}$  to  $5 \times 10^{-2}$  W/kg in the surf zone for water depths of 0.3 to 3 m and offshore significant wave heights of 0.5 to 1.2 m. The smaller values corresponded to lower percentages of broken waves and to smaller ratios of wave height to water depth. Also for the surf zone, Trowbridge and Elgar [2001] have reported  $\epsilon$  values reaching several times  $10^{-4}$  W/kg under 1- to 3-m significant wave heights in ca. 4- to 5-m water depths, the highest values being associated with 0.5- to 1-m/s longshore currents. For water depths less than 2.5 m both within and outside the surf zone, Bryan et al. [2003] obtained values ranging from  $3 \times 10^{-5}$  to  $3 \times 10^{-3}$  W/kg for  $H_s$  between 0.1 and 0.6 m. Within the surf zone, the higher values corresponded to shallower water depths and higher waves. Outside the surf zone,  $\epsilon$  decreased with increasing water depth, decreasing wave height, and increasing wave period. Foster et al. [2006] obtained wave phase resolved values of  $\epsilon$  as high as  $10^{-3}$  W/kg under mostly unbroken 4.5-s waves in 2-m water depth on the seaward side of the crest of a longshore sandbar.

[63] The  $0.1 \times 10^{-6}$  to  $3 \times 10^{-6}$  W/kg values of  $\epsilon$  obtained here for 17-m water depth and 1-m significant wave heights are 1 to 2 orders of magnitude less than the lowest estimates cited above. Given the relatively small ratio of wave height to water depth, small values of  $\epsilon$  are certainly expected within the water column. Furthermore, for the 6-s wave periods relevant here,  $kh = 2.0$  so the waves were effectively in deep water (i.e.,  $kh > 1.75$ , Kundu [1990]). Thus while dissipation rates should increase as the bed is approached, the fact that near-bed values of  $\epsilon$  would be this small for moderate-amplitude deep-water waves is not surprising. The present range of  $\epsilon$  values is also comparable to the  $10^{-7}$  to  $10^{-5}$  W/kg range observed by Gross et al. [1994] in ca. 100-m water depth on the California shelf during the winter storm season.

### 6.2. The Structure Function

[64] The above-cited measurements were made with point sensors: i.e., hot-film anemometers [George et al., 1994; Foster et al., 2006]; single-point acoustic Doppler velocimeters [Trowbridge and Elgar, 2001; Bryan et al., 2003]; or acoustic traveltime sensors [Gross et al., 1994]. One advantage of profiling systems over single-point methods is that the instantaneous velocity profile enables estimates of the dissipation to be obtained via the vertical structure

function, and thus without having to invoke Taylor's hypothesis. This advantage has been pointed out previously by *Veron and Melville* [1999], who used a very similar system to estimate dissipation under waves within ca. 0.5 to 2 m of the sea surface. *Veron and Melville* [1999] computed the turbulence wave number spectrum directly from the Fourier transform of the along-beam velocity. The direct wave number spectrum approach could not be implemented here because a multiple reflection at roughly 13- to 15-cm height limited the useable length of the velocity profile. (Incidentally, *Veron and Melville* [1999] obtained quasi-instantaneous values of  $\epsilon$  up to  $5 \times 10^{-4}$  W/kg under breaking waves, and time-averaged values of  $O(10^{-5})$  and  $O(10^{-4})$  W/kg for 0.7- and 1.8-m significant wave heights. These rates are comparable to those cited above, and the lower value is similarly an order of magnitude higher than the highest value reported here.)

[65] *Veron and Melville* [1999] estimated the near-surface dissipation rates both from the wave number spectrum and using the mean strain rate along the profile: that is, via the relationship [*Tennekes and Lumley*, 1972]

$$\epsilon_{SR} = 15\nu \langle [dw/dz]^2 \rangle. \quad (22)$$

Comparing this expression with equation (6), it is clear that both depend on the mean square along-beam velocity difference. Estimates of  $\epsilon$  based on equation (22) for the present data set are comparable to those in Figure 8. However, viscosity should not affect the strain rate in the inertial subrange [*Monin and Yaglom*, 1971], so this agreement must be coincidental. Indeed, taking the ratio of two expressions,  $\epsilon_{SR}/\epsilon_{SF} = [15\nu 2^{3/2}/\Delta z] / [\langle \Delta w^2 \rangle^{1/2}]$ , and substituting  $\langle \Delta w^2 \rangle \sim 0.2$  to  $0.4$  cm<sup>2</sup>/s<sup>2</sup> at  $\Delta z = 0.7$  cm (Figure 11), gives  $\epsilon_{SR}/\epsilon_{SF} \sim 1.7$  to  $1.2$ .

[66] The structure function estimates of dissipation include a contribution at the wind-wave frequency (Figure 11). Some of this energy might be due to vertical shear and/or vertical strain within the wave bottom boundary layer, as opposed to turbulence. For rough turbulent flow, the WBBL thickness  $\delta$  is given  $K\kappa u_*/\omega$ , where  $\kappa = 0.4$  is von Karman's constant, and  $K = 2$  for an outer measure of the thickness [*Grant and Madsen*, 1979, 1986]. With  $u_* = 0.5$  cm/s, and  $T_p = 6$  s,  $\delta \sim 0.4$  cm which is less than the 0.7-cm thickness of the CDP range bins. Recall that the structure functions were computed using both 0.7-cm and 1.4-cm as the height of the first bin, with little difference in the resulting values of  $\epsilon$  (Figure 9). Combined with the 0.4-cm estimate for  $\delta$ , this result suggests that shear within the WBBL did not contribute significantly to the structure function estimates.

[67] Additional near-bed shear and strain might also be induced by ripple-induced perturbations to the interior potential flow. *Davies* [1983] has derived an analytic solution for oscillatory potential flow over sinusoidal ripples which is applicable when wave orbital excursions are less than the ripple wavelength, and when flow-separation does not occur. Both conditions are satisfied here. That is,  $T_p = 6$  s and  $\tilde{u}_b = 5$  cm/s give  $2A_{1/3} \sim 20$  cm, which is less than half the 50-cm ripple wavelength. Also, by YD294 the RMS ripple elevation had decayed to 1.3 cm, corresponding to a (sinusoidal) ripple amplitude  $a = \eta_R/2 = 1.8$  cm and therefore a ripple steepness  $\eta_R/\lambda$  of about 0.07, which is

small compared to the value of 0.2 for equilibrium orbital ripples. Considering as well that the mean wave direction during this period was ca.  $200^\circ$  and therefore at a  $40^\circ$ -angle to the ripple crests, the ripple wavelength in the direction of wave motion would have been about 70 cm and the corresponding values of effective ripple steepness and excursion-to-wavelength ratio even smaller. From *Davies'* solution, the maximum RMS amplitudes along the ripple profile of the vertical and horizontal velocities are given by

$$\tilde{w}(z) = \tilde{u}_b a k_r \exp(-k_r z) \quad (23)$$

and

$$\tilde{u}(z) = \tilde{u}_b [1 + a k_r \exp(-k_r z)], \quad (24)$$

where  $k_r = 2\pi/\lambda$  is the ripple wave number. With the vertical strain rate of the wave motion,  $d\tilde{w}(z)/dz$ , taken from equation (23),  $(\Delta\tilde{w})^2$  was computed at the same vertical separations as the structure function. The results for  $a = 1.8$  cm,  $\lambda = 50$  cm, and  $\tilde{u}_b = 5$  cm/s are the + -points plotted in Figure 10. Recalling that the CDP was tilted at an angle  $\beta = 5^\circ$  away from vertical, the contribution to  $\Delta\tilde{w}$  from vertical shear is  $\sin\beta [d\tilde{u}(z)/dz] \Delta z$ . The open circles in Figure 10 are the resulting values of  $(\Delta\tilde{w})^2$ . The contribution from vertical shear is negligible, while that from the vertical strain rate apparently could become important at the larger separations. Recall that equations (23) and (24) represent the maximum contributions along the ripple profile. For equation (23), this maximum occurs where the bottom slope is greatest: i.e., at the zero-crossings. On the basis of the relative positions of the fanbeam and CDP1 on the frame, and the  $5^\circ$  offshore tilt of the CDP1 beam, the best estimate of the intersection point of the CDP1 beam and the ripple profile is close to a ripple crest (ca. 5 cm southwest of the  $x = 2$  m,  $y = 1$  m grid point in Figure 12). The margin of error in this estimate is rather large, however, as the local bed geometry is complicated by the sinuosity of the ripple crest, a secondary ripple at the half-wavelength of the primary, and nearby fishpits.

### 6.3. Noise Levels

[68] In pulse-coherent Doppler systems, the correlation and velocity standard deviation are related by [*Zedel et al.*, 1996]:

$$\sigma_w = \frac{c_a}{\omega_a \tau_a} \left[ \frac{1}{2} \log \frac{1}{R^2} \right]^{1/2}, \quad (25)$$

where  $\sigma_w$  is the velocity standard deviation,  $c_a$  the speed of sound,  $\tau_a$  the pulse separation time, and  $R^2$  the magnitude of the complex correlation between the received signals from the two pulses. During the period of interest (YD293-296), the run-mean values of  $R^2$  ranged from 0.73 when the  $\epsilon_{SF}$  was high, to 0.94 when it was low. Substituting  $R^2 = 0.94$  in equation (25) gives a variance of  $0.11$  cm<sup>2</sup>/s<sup>2</sup>. This is in good agreement with the variance obtained by integrating  $1.1 \times 10^{-2}$  cm<sup>2</sup>/s<sup>2</sup>/Hz, the background noise level in Figure 7a, across the width of the spectrum.

[69] However, the noise variance above is a factor of 10 larger than expected on the basis of measurements in still

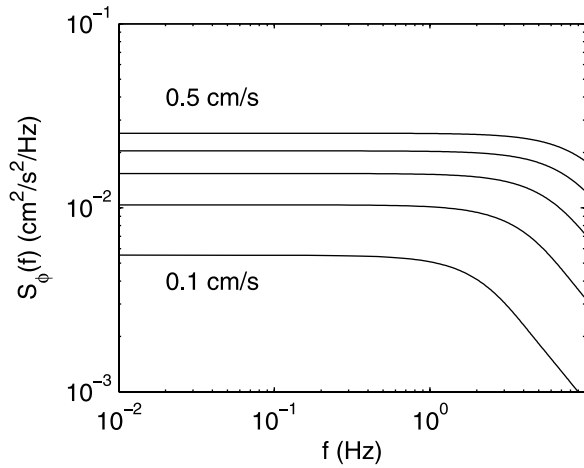


**Figure 22.** Predicted ambiguity spectra at 1.7 MHz acoustic frequency for different values of  $[\Delta w'^2]^{1/2}$  in 0.1 cm/s steps.

water [Zedel *et al.*, 1996]. It is likely that the higher noise level is due to decorrelation by small-scale turbulence within the CDP sampling volume. Garbini *et al.* [1982a] derived relationships for the effects of small-scale turbulence and advection on the velocity spectrum measured with pulse-coherent Doppler, and verified their theoretical expressions with experiments in both laminar and turbulent flow [Garbini *et al.*, 1982b]. Since the velocity estimate is based on the time rate of change of phase, individual estimates can be written as the sum of two terms,

$$w = \langle w \rangle + \frac{k_a}{2} \frac{d\Phi}{dt}, \quad (26)$$

where  $\langle \rangle$  denotes the spatial average over the detected volume,  $\Phi$  is the phase “noise”, and  $k_a$  is the wave number of the transmitted sound. The first term represents the average over the along-beam pulse-to-pulse displacements of the scatterers within the detected volume, the second the departure from this average due to turbulent reconfiguration of particle positions within the volume and to advective exchange of particles at the boundaries of the volume. The measured spectrum is thus represented as the sum of two contributions

$$S_{ww} = S_{\langle w \rangle} + S_\phi, \quad (27)$$

where  $S_{\langle w \rangle}$  is the true spectrum of the volume-averaged velocity, and  $S_\phi$  is the spectrum of the phase noise, the so-called ambiguity spectrum. Garbini *et al.* [1982a] have derived a theoretical expression for the ambiguity spectrum which, when written as a velocity power spectrum takes the form:

$$S_\phi(f) = \pi^{3/2} \frac{k_a^2 \Delta}{4} \sum_{n=1}^{\infty} n^{-3/2} \exp\left[\frac{\pi^2 f^2}{n \Delta^2}\right], \quad (28)$$

where

$$\Delta^2 = 0.5 \overline{\langle u_i \rangle^2} / L_i^2 + k_a^2 \overline{\Delta w'^2}, \quad (29)$$

$\bar{X}$  denoting the time average of quantity  $X$  over many pulse pairs. The first term on the right in equation (29) is the contribution from particle advection through the boundaries of the detected volume, with  $i = 1, 2, 3$  the Cartesian coordinate index, and  $L_i$  the characteristic dimension of the detected volume in the  $i$ th direction. The second term is due to scatterer reconfiguration within the volume by turbulence. The time-mean of the mean square departure of  $w$  from its spatial average is denoted by  $\overline{\Delta w'^2}$ , and is related to the true turbulence intensity  $\overline{w'^2}$  by

$$\overline{\Delta w'^2} = \overline{w'^2} - \overline{\langle w \rangle'^2}, \quad (30)$$

where  $\overline{\langle w \rangle'^2}$  is the variance of the spatially averaged fluctuations.

[70] The above results were derived assuming a Gaussian-shaped detected volume in all 3 dimensions, and so do not strictly hold in the present case. However, for reasonable values of the parameters involved here, the turbulence term in equation (29) dominates. That is, noting from equation (30) that  $\overline{\Delta w'^2}$  must be less than the true turbulence intensity, set  $[\Delta w'^2]^{1/2} = 0.1$  cm/s (section 5.1). Then, with 5 cm/s and 1 cm/s as upper bounds for the RMS horizontal and vertical advection speeds, and with  $2L_1 = 3$  cm and  $2L_3 = 0.7$  cm for the horizontal and vertical length scales of the detected volume, the vertical and horizontal advection terms are each a factor of 10 smaller than the turbulence term in equation (29). Thus the dependence of  $S_\phi(f)$  on the detected volume shape should be relatively weak.  $S_\phi(f)$  was computed using the above values for the advection parameters and  $[\Delta w'^2]^{1/2}$  ranging from 0.1 to 0.5 cm/s. The resulting ambiguity spectra (Figure 22) exhibit nearly flat plateaus at low frequencies followed by rapid decay at high frequencies. The plateau levels are quite comparable to the “noise” levels in the observed energy spectra (Figure 7) and extend over the correct range of frequencies, especially for  $[\Delta w'^2]^{1/2} = 0.2$  cm/s. Given the approximate representation of the CDP detected volume in the theory, this qualitative and quantitative agreement seems very compelling, and leads to the conclusion that the apparent noise levels in the observed  $S_{ww}$  spectra were almost certainly due to the turbulence-driven reconfiguration of the scatterers within each range bin from pulse to pulse.

[71] Garbini *et al.* [1982a] also suggest a method for estimating the true (spatially averaged) energy spectrum based on measurements at two spatially separated locations. The idea is that the ambiguity phase fluctuations at the two positions are uncorrelated, and therefore only the spatially averaged velocities contribute to the lagged cross-correlation function [Garbini *et al.*, 1982a, equations (3.1) and (3.2)]. Because the structure function is based on the difference between velocity measurements at spatially separated points, it is interesting to consider the contribution of the ambiguity spectrum to the spectrum of the velocity differences. Since the cross-spectrum is the Fourier transform of the cross-correlation function, the difference spectrum becomes

$$S_{\Delta w \Delta w} = S_{w_1 w_1} + S_{w_2 w_2} - 2\Re[S_{w_1 w_2}], \quad (31)$$

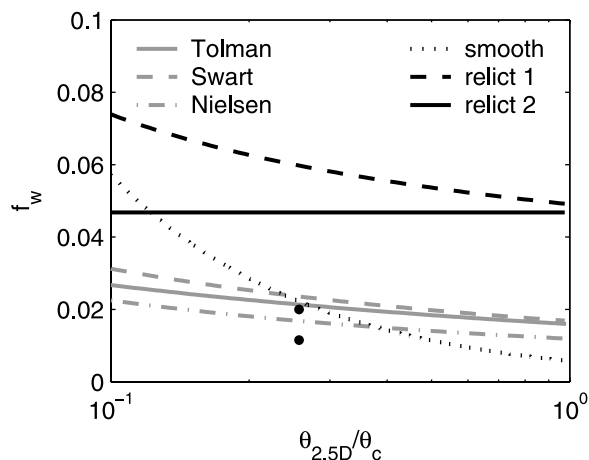


**Figure 23.** Wave friction factors in the relict ripple zone versus Shields parameter ratio,  $\theta_{2.5D}/\theta_c$ , for 405- $\mu\text{m}$  diameter sand and 6-s period waves. The dotted line is the smooth wall curve.

where  $\Re$  denotes the real part, so the last term is the twice the co-spectrum. Making the *Garbini et al.* [1982a] argument, the co-spectrum should equal  $S_{(w)1}$ , provided the two points are close enough and there is no shear or strain at the separation scale.  $S_{\Delta w \Delta w}$  would then reduce to  $2S_\phi$  which, as Figure 22 indicates, is unlike the velocity difference spectra (Figure 11) in either shape or  $\Delta z$ . ( $S_\phi$ -dependence would be independent of separation in homogeneous turbulence.) The implication is that strain must therefore have been present at 0.7- to 3.5-cm separations, which is encouraging, as otherwise the structure function should have yielded a null result.

#### 6.4. Turbulence Intensity

[72] The observed wave friction factors are somewhat small, as even those based on the significant wave orbital velocity amplitude (the solid black points in Figure 21) fall on or slightly below the smooth wall relation. From equation (10), a 40% increase in  $\sigma'_w$  would double the observed values of  $f_w$  and so raise the smaller of the two observed points to the smooth wall curve. The implication is that the turbulence intensities have been underestimated by roughly a factor of two. One possible contributor to an underestimate of  $\sigma'_w$  is the spike removal technique. If it is supposed that the spikes were in fact real, then the 2% average rejection rate would imply that the standard deviation of the discarded data would need to be only about 2.6 times that of the data retained to double the overall variance. So, despite the fact that isolated and apparently erroneous spikes are present in the raw CDP time series, it is possible and even probable that real high-amplitude velocity fluctuations were unavoidably discarded as well.

[73] A more likely explanation for  $\sigma'_w$  being underestimated, however, is spatial averaging over the turbulence within the CDP range bins. From equation (30), with  $[\overline{\Delta w^2}]^{1/2} = 0.2 \text{ cm/s}$  (section 6.3), and  $[\langle w \rangle^2]^{1/2} = \sigma_w$ , i.e., the 0.22-cm/s measured value (section 5.1), it is seen that the true turbulence intensity could easily be double the observed estimate.

#### 6.5. Relict Ripple Roughness

[74] *Tolman* [1994] suggested that the roughness of relict ripples be assigned a constant value of 1 cm. On the basis of their model-data comparisons for wave attenuation across the shelf, however, *Ardhuin et al.* [2003a, 2003b] concluded that the apparent roughness should increase with wave energy, and proposed that

$$k_N = \max[1 \text{ cm}, a_4 A], \text{ (relict ripples)} \quad (32)$$

where  $A$  is the RMS orbital semi-excursion, and  $a_4$  is a constant with a best fit value of 0.05.

[75] Various predicted friction factors in the relict ripple zone (i.e.,  $\theta_{2.5} < \theta_c$ ) are shown in Figure 23 for 6-s waves and 405- $\mu\text{m}$  median grain diameter sand. The grey curves represent the friction factor for fixed-grain roughness. Note that the Tolman and Swart curves are nearly identical, especially as  $\theta_{2.5}/\theta_c$  approaches unity. This near equivalence allows the effect of equation (32) on  $f_w$  to be considered directly without having to invoke the implicit boundary layer equations. Thus substituting (32) in equation (14) (or equation (15)), it is seen that  $f_w$  assumes a constant value if  $a_4 A$  exceeds 1 cm, and otherwise decreases with increasing  $A$  and  $\theta$  [see *Ardhuin et al.*, 2003a, Figure 1]. The relict ripple curves in Figure 23 illustrate both behaviors. These curves were computed using equation (32) for  $r$  in equation (14) with 2 values for the constant roughness: the 1 cm suggested by Tolman, and 0.2 cm. The curve for smaller roughness is required to obtain the dependence of relict roughness on wave energy indicated by the *Ardhuin et al.* [2003b] results, and is arguably in better agreement with SAX04 results. Note that the *Ardhuin et al.* [2003b] observations were of long-period swell ( $T_p \sim 12 \text{ s}$ ) with 1-m significant wave heights in water depths of 8- to 40-m. The nearbed orbital excursions for such waves would have been 1 to 1.2 m at mid-shelf (17- to 22-m depth). With these large orbital excursions and m-scale wavelength ripples, one could expect that the physical roughness of the bed would be comparable to the ripple height (i.e.,  $O(1) \text{ cm}$ ). For the present data set, however, the orbital excursions were much less than the ripple wavelength (section 6.2), and the same reasoning therefore suggests that the physical roughness appropriate for these conditions would be associated with features smaller than the ripple scale. Thus these comparisons indicate a probable dependence of relict ripple roughness on the ratio of the nearbed orbital excursion to the ripple wavelength, and therefore on wave period as well as wave energy.

[76] Comparing Figure 23 to Figure 21, one sees that the previously suggested expressions for relict-ripple roughness lead to an abrupt discontinuity in the predicted friction factor at  $\theta = \theta_c$ , whereas the roughness given by Nielsen's expression allows for a smooth transition across this boundary. Which of these very different dependencies is more appropriate is an open question, but the smooth transition would seem to be more realistic physically.

#### 6.6. Ripple Decay: Physics Versus Biology

[77] There is little evidence that physical decay processes had any significant effect on the ripple field during the post-Matthew period, except possibly early in the record when mean currents were strongest (Figure 3). The break in the

data record at this time (due to the ship disconnecting from the mooring) is unfortunate in this respect, since a short period of more intense near-bed forcing may have occurred and been missed. However, the fan beam images of the seabed acquired immediately before and after the break do not indicate that any reorganization of the ripple field occurred.

[78] The bed elevation spectra (Figures 17 and 19) exhibit growth at spatial frequencies below 2 cpm beginning on or about YD301. This change might suggest a reorganization of the ripple pattern. However, there was no concurrent increase in the wave and current forcing conditions to drive such a reorganization (Figures 3 through 6). Furthermore, the fanbeam imagery for the period YD301-306 do not exhibit evidence for reorganization at these scales, indicating instead the persistence of the 2-cpm primary ripples in their post-Matthew configuration. The fanbeam images do show the formation of a ca. 50-cm pit, presumably the work of a fish, along the line of the pencil-beam profile. Thus the altered character of the bed elevation spectra and increased bed elevation variance following YD301 were the result of biological activity, not physics.

## 7. Summary and Conclusions

[79] Observations have been presented of hydrodynamic forcing, including near-bed turbulence, and the decay of waveformed sand ripples on the inner shelf. The measurements were made in 17-m water depth during a 19-d period of relatively quiescent conditions following the passage of Tropical Storm Matthew. Typical current speeds during this period were less than 10 cm/s, and typical RMS wave orbital velocities 5 cm/s or less, associated with 6-s period waves and 1-m maximum significant wave heights. The wavelengths of the primary ripples formed during the tropical storm were 50–60 cm, with heights of about 5 cm at the start of the observation period. Within 15 days of that time, RMS ripple elevation had decreased by a factor of 2, from about 1.8 to about 0.7 cm. The ripple degradation timescale, defined as the time taken for the bed elevation variance of the 50-cm wavelength primary ripples to decrease by 50%, was about 8 days. The primary degradation mechanism involved fish making pits in the seafloor.

[80] Near-bed turbulent kinetic energy dissipation rates are estimated both from the energy spectrum and from the vertical structure function within the inertial subrange, and ranged from  $0.1 \times 10^{-6}$  to  $3 \times 10^{-6}$  W/kg. This range is 1 to 2 orders of magnitude less than previous minimum values of time-averaged dissipation rates measured under  $O(1)$ -m height sea-and-swell waves. However, these earlier measurements were made in much shallower water, whereas the waves here are effectively in deep water ( $kh = 2$ ), so much smaller dissipation rates are to be expected. The friction velocity at the bed, determined from the near-bed turbulence intensities and from the dissipation rates, ranged from 0.3 to 0.5 cm/s. The corresponding estimates of the wave friction factor, relative to the significant wave orbital velocity, ranged from 0.017 to 0.02. The maximum estimated value of the grain roughness Shields parameter (based on the significant wave orbital velocity and on a grain roughness of  $2.5D_{50}$ ) was 0.013, well below the critical threshold for grain motion. These results indicate that movement of

sediment grains in response to fluid forcing would have occurred only occasionally under the action of the highest waves and the largest turbulence fluctuations, consistent with the dominant ripple degradation mechanism being biological re-working of the surficial sediments.

[81] It is likely, however, that the nearbed turbulence intensities and consequently the estimated values of  $f_w$  are too small by roughly a factor of 2. Two independent lines of argument lead to this inference, one based on the noise levels in the Doppler sonar data, the other on the values of the friction factor relative to that predicted for a smooth wall. Given the 405- $\mu\text{m}$  median grain size of the surficial sediments, and the small-scale bed roughness associated with the fish pits, the seabed could not have been hydraulically smooth. The observed values of  $f_w$ , however, fall on or below the smooth-wall  $f_w$  versus  $\theta_{2.5}$  curve, indicating that the observed values must be underestimates. The second argument uses the theoretical ambiguity spectrum, as derived by *Garbini et al.* [1982a] for pulse-coherent acoustic Doppler systems, to demonstrate that the apparent noise levels in the near-bed vertical velocities were primarily due to turbulent reconfiguration of scatterers within the detected volume from pulse to pulse. The velocity variance associated with the noise is then a measure of the difference between the true turbulence intensity variance and the variance of the spatially averaged velocities registered by the Doppler system. It follows that the sum of the integral of the power spectrum over the noise-corrected inertial subrange, and the integral of the phase noise over the full width of the spectrum, provides an estimate of the true turbulence intensity. Plausible values yield a factor of two increase in the observed turbulence intensities, and therefore to a factor of 2 increase in the numerical values of  $f_w$  reported here.

[82] The question of the effective roughness of relict ripples is examined in the light of the above results. In agreement with *Ardhuin et al.* [2003a], the constant value of 1 cm suggested by *Tolman* [1994] does not appear to be adequate. On the basis of comparisons between observed and model-predicted attenuation of long-period swell, *Ardhuin et al.* [2003a] concluded that the roughness should depend upon wave energy and represented that dependence as a proportionality to wave orbital excursion. The results presented here for short-period waves suggest the likely importance of the orbital excursion relative to the ripple wavelength, and thus indicate an additional dependence on wave period. Also, the ripple roughness parameterization suggested by *Nielsen* [1992] is shown to yield trajectories in  $f_w$ - $\theta$  space with endpoints encouragingly close to the observations (especially if the observed friction factors are corrected upward by a factor of 2). Nielsen's roughness formula is proportional to the product of ripple height and steepness, with the constant of proportionality determined from experiments with equilibrium ripples. The results here indicate a ca. 25% reduction in the value of this constant, the suggestion being that irregular waves and non-equilibrium effects associated with the time-history of the wave forcing during storm events lead to an initial relict ripple state with lower roughness than equilibrium ripples generated by regular waves.

[83] As anticipated, the instrument frame served as a fish refuge, leading to accelerated (and therefore measurable) rates of biologically driven ripple decay during a period of

relatively quiescent forcing conditions. The fish-seabed interactions themselves are likely to be representative of a natural process, since the observed pit-making behavior would presumably occur in the absence of the instrument frame. Extrapolating the observed decay rates to natural fish population densities would be worthwhile and possible in principle, given a suitable model of the degradation process. This is a topic for future study.

[84] In conclusion, the results from this first investigation of turbulence over degrading sand ripples indicate that the hydraulic roughness of relict ripples is likely a function of both ripple height and steepness, and that the relative roughness should also depend on the near-bed wave orbital excursion. For modeling purposes, Nielsen's ripple roughness formula is recommended since it incorporates both ripple height and steepness, together with one of the standard approaches for estimating  $f_w$  from roughness and orbital excursion, at least until measurements over a wider range of conditions become available. The results also indicate that the proportionality constant in Nielsen's formula should be reduced to account for the more rounded crests of ripples formed in irregular waves (as suggested by *Madsen et al.* [1990]) and non-equilibrium response [*Traykovski et al.*, 1999]. An additional factor may be needed to account for ripple age, but the factor of 2 uncertainty in  $f_w$  precludes a definite conclusion on this point. From the standpoint of near-bed turbulence measurements in the field using coherent Doppler sonar, the structure function method for estimating dissipation rates appears to be quite promising, and worth pursuing in future. Similarly, the ambiguity spectrum appears to offer an interesting approach for determining true turbulence intensities from the spatially averaged values within each range cell.

## Appendix A

[85] Assuming locally homogeneous, isotropic turbulence and unidirectional flow, the turbulent kinetic energy dissipation rate is [*Tennekes and Lumley*, 1972, pp. 252–265]

$$\epsilon = 2\pi \left[ \frac{55}{36} \right]^{3/2} \frac{S_{ww}^{3/2}(f)}{\bar{U}} f^{5/2}, \quad (\text{A1})$$

where  $S_{ww}(f)$  is the power spectral density of  $w$  in the inertial subrange and  $\bar{U}$  is the mean flow speed used to convert wave number to frequency via Taylor's frozen turbulence hypothesis: i.e.,  $\omega = k\bar{U}$ . Note that in equation (A1), and in the spectral relations below involving  $\epsilon$ , the Kolmogorov constant has been set equal to 1.5 [*Tennekes and Lumley*, 1972, p. 265; *Pope*, 2000, p. 233]. Note also that  $S_{ww}$  here is a single-sided spectral density, defined for positive frequencies only, whereas the spectra used by Tennekes and Lumley were defined over both positive and negative frequencies (compare, for example, equation (8.1.6) by *Tennekes and Lumley* [1972] to equation (3)–(49) by *Hinze* [1975]). Comparing equation (A1) to equation (5), it is seen that  $B_w = 2\pi[15/18]^{3/2}$ , and hence  $B_w = 11.9$ .

[86] *Lumley and Terray* [1983] derived expressions for the turbulence spectrum close to the sea surface for random deep-water waves propagating in the same direction as the

mean current. Noting that *Lumley and Terray* used two-sided spectra (their equation (3.5)), and that  $S_{uu} = S_{ww}$  for unidirectional deep-water waves and zero mean flow, their equation (4.5) for the  $\bar{U} = 0$  case can be re-written as

$$\epsilon = 2\pi \left[ \frac{110}{63} \right]^{3/2} \frac{S_{ww}^{3/2}(f)}{\sigma_o} f^{5/2} \quad (\text{A2})$$

where  $\sigma$  is the RMS wave orbital velocity and the subscript  $o$  denotes the value at the sea surface. This equation gives  $B_{wo} = 2\pi[110/63]^{3/2} = 14.5$ .

[87] *Lumley and Terray* [1983] obtained a second expression applicable to a random wavefield, their equation (4.7), by averaging over Rayleigh-distributed wave amplitudes. When recast in the form above, this expression becomes

$$\epsilon = 2\pi \left[ \frac{110}{21\Gamma(1/3)2^{1/3}} \right]^{3/2} \frac{S_{ww}^{3/2}(f)}{\sigma_o} f^{5/2} \quad (\text{A3})$$

giving  $B_{wo} = 12.1$ .

[88] *Trowbridge and Elgar* [2001] adapted the theoretical treatment of *Lumley and Terray* [1983] to the near-bed region by setting  $\bar{W}$  and  $\tilde{w}$  to zero, and obtained an expression for  $S_{ww}$  for combined wave-current flows, their equation (7). Noting their use of two-sided spectra, their expression when re-arranged becomes

$$\epsilon = 2\pi \left[ \frac{55}{36F} \right]^{3/2} \frac{S_{ww}^{3/2}(f)}{\sigma} f^{5/2}. \quad (\text{A4})$$

The factor  $F$  is a function of the relative strength and direction of the waves and current, and is based on equation (A13) in *Trowbridge and Elgar* [2001]: that is,

$$I(\bar{U}/\sigma, \phi)^{-3/2} = \frac{\bar{U}}{\sigma} F(\bar{U}/\sigma, \phi)^{-3/2} \quad (\text{A5})$$

where

$$F(\bar{U}/\sigma, \phi) = \frac{1}{\sqrt{2\pi}} \int_{-\infty}^{\infty} \left[ \xi^2 - 2\frac{\bar{U}}{\sigma} \xi \cos \phi + \frac{\bar{U}^2}{\sigma^2} \right]^{1/3} \cdot \exp(-\xi^2/2) d\xi, \quad (\text{A6})$$

and  $\xi$  is a non-dimensional frequency. Note that in these expressions,  $\sigma$  is the RMS orbital velocity near the bed and hence is identical to  $\tilde{u}_b$ . For  $\bar{U}/\sigma = 0$ , numerical integration of equation (A6) gives  $F = 1.39$ . Thus for the zero mean current case,  $B_w = 2\pi[55/(36F)]^{3/2} = 7.23$ .

[89] *Bryan et al.* [2003], also following the *Lumley and Terray* [1983] treatment, obtained an expression for the spectrum of turbulence beneath monochromatic waves in arbitrary water depth and zero mean flow. The spectrum is expressed as a Fourier series of harmonics of the wave angular frequency  $\tilde{\omega}$ . For the vertical component, their equation (13) can be rewritten as

$$S_{n3} = \frac{1.5\Gamma(2/3)}{\Gamma(1/3)\Gamma(4/3)} G(z) \left( \frac{\epsilon \tilde{U}_b}{2} \right)^{2/3} \tilde{\omega}^{-5/3} \frac{\Gamma(n-1/3)}{\Gamma(n+4/3)} \quad (\text{A7})$$

where  $\tilde{U}_b$  is the wave orbital velocity amplitude at  $z = -h$ ,  $n = \omega/\tilde{\omega}$ , and  $G$  is a depth-dependent double integral over the polar and azimuthal angles in wave vector space:

$$G = \frac{1}{4\pi} \int_0^{2\pi} \int_0^\pi \left\{ (1 - \sin^2 \theta_k \sin^2 \vartheta_k) \sin^{5/3} \vartheta_k \times [\cos^2 \theta_k \cosh^2 \tilde{k}(z+h) + \sin^2 \theta_k \sinh^2 \tilde{k}(z+h)]^{1/3} \right\} d\vartheta_k d\theta_k, \quad (\text{A8})$$

where  $\tilde{k}$  is the wave number of the waves. At the seabed,  $z = -h$ , this integral can be solved analytically [Gradshteyn and Ryzhik, 1980, p. 369; Abramowitz and Stegun, 1965, pp. 255–256] yielding

$$G_b = \frac{1}{2\pi} \frac{1}{165} \left[ \frac{2^{2/3} \Gamma(-1/6) \Gamma(1/3)}{\Gamma(2/3)} \right]^2 = 0.436. \quad (\text{A9})$$

[90] The second ratio of Gamma functions in equation (A7) can be written as [Abramowitz and Stegun, 1965, p. 256]

$$\frac{\Gamma(n-1/3)}{\Gamma(n+4/3)} = \frac{9\Gamma(2/3)}{4\Gamma(1/3)} \prod_{m=2}^n \frac{3m-4}{3m+1} \quad (\text{A10})$$

for  $n \geq 2$ . A log-log fit to either side of this equation over values of  $n$  ranging from 2 to 100 gives  $1.01 n^{-1.669}$ , close enough to  $1.0 n^{-5/3}$  for the present purposes [see Lumley and Terray, 1983, equation (3.4)]. Thus at the seabed equation (A7) becomes

$$S_{ww}(\omega) = 3G_b \left( \frac{\epsilon \tilde{U}_b}{2} \right)^{2/3} \frac{\Gamma(2/3)}{\Gamma(1/3)\Gamma(4/3)} \omega^{-5/3}, \quad (\text{A11})$$

the additional factor of 2 again accounting for conversion from two-sided to single-sided spectral densities [see Bryan et al., 2003, equation (9)]. Hence

$$\epsilon = 4\pi \left[ \frac{\Gamma(1/3)\Gamma(4/3)}{3\Gamma(2/3)G_b} \right]^{3/2} \frac{S_{ww}^{3/2}(f)}{\tilde{U}_b} f^{5/2}. \quad (\text{A12})$$

Replacing  $\tilde{U}_b$  with the energy-equivalent RMS wave amplitude  $\sqrt{2}\tilde{u}_b$  yields  $B_w = 13.9$ .

[91] Equation A8 can also be used to obtain a result for the dissipation rate at the sea surface for comparison to equation (A12) and to the Lumley and Terray results. For  $kh = 2$  (corresponding to  $h = 17$  m and  $T_p = 6$  s), numerical integration gives  $G_o = 1.27$ . With  $\tilde{U}_b$  in equation (A12) replaced by  $\sigma_o$ ,  $B_{wo} = \cosh kh [G_b/G_o]^{3/2} B_w$ , or  $B_{wo} = 10.7$ .

[92] Thus the different values predicted for  $B_w$  near the seabed range from 7.2 to 13.9, with a mean value of about 10. Interestingly, the range of  $B_w$  for the near-bottom region is not very different from the 10.7 to 14.5 range for  $B_{wo}$  at the sea surface, at least not in the present context given the scatter in the estimates of  $\epsilon$ .

[93] Finally, consider the likely effect of the mean current on  $\epsilon_{Sp}$  in the present data set. The Vector-measured mean speeds and the pressure-based estimates of  $\tilde{u}_b$  (Figures 3 and 6),  $U/\tilde{u}_b$  ranged from 0.012 to 0.15 for the period of primary

interest, YD293-295. Since the Vector measurements were at 50-cm height, where mean speeds would be greater than those at the 2- to 12-cm heights of the CDP measurements, these values of  $U/\tilde{u}_b$  are overestimates. Numerical integration of equation (A6)  $U/\tilde{u}_b < 0.15$  yields values of  $F^{-3/2}$  between 1.33 and 1.39 for the range of  $\phi$  relevant here (ca.  $60^\circ$  to  $130^\circ$ ), compared to 1.39 for  $U/\tilde{u}_b = 0$ . Thus the correction to  $\epsilon$  introduced by accounting for advection by the mean current is expected to be less than 5%, justifying the substitution of  $\tilde{u}_b$  for  $U$  in equation (5).

[94] **Acknowledgments.** The author is grateful to the captain and crew of R/V *Seward Johnson*, to Mike Richardson and his team of divers, to Eric Thorsos, Chief Scientist for SAX04, to Walter Judge, Matt Hatcher, Ryan Mulligan, Doug Schillinger, Richard Dittman, and Chris L'Esperance for assistance with the field effort, to Robert Craig for upgrades to the data acquisition software, and to Len Zedel for useful discussions of Doppler sonar performance. This work was funded by the U.S. Office of Naval Research Coastal Geosciences Program.

## References

- Abramowitz, M., and I. Stegun (1965), *Handbook of Mathematical Functions*, Dover Press, New York.
- Arduin, F., T. Herbers, P. F. Jessen, and W. O'Reilly (2003a), Swell transformation across the continental shelf. Part II: Validation of a spectral energy balance equation, *J. Phys. Oceanogr.*, *33*, 1940–1953.
- Arduin, F., W. O'Reilly, T. Herbers, and P. F. Jessen (2003b), Swell transformation across the continental shelf. Part I: Attenuation and directional broadening, *J. Phys. Oceanogr.*, *33*, 1921–1939.
- Bryan, K. R., K. P. Black, and R. M. Gorman (2003), Spectral estimates of dissipation rate within and near the surf zone, *J. Phys. Oceanogr.*, *33*, 979–993.
- Clifton, H. E., and J. R. Dingler (1984), Wave-formed structures and paleoenvironmental reconstruction, *Mar. Geol.*, *60*, 165–198.
- Davies, A. G. (1983), Wave interactions with rippled sand beds, in *Physical Oceanography of Coastal and Shelf Seas*, edited by B. Johns, pp. 9–19, Elsevier, New York.
- Foster, D., R. Beach, and R. Holman (2006), Turbulence observations of the nearshore wave bottom boundary layer, *J. Geophys. Res.*, *111*, 004011, doi:10.1029/2004JC002838.
- Fredsoe, J., and R. Deigaard (1992), *Mechanics of Coastal Sediment Transport*, World Scientific, 369 pp.
- Garbini, J. L., F. K. Forster, and J. E. Jorgensen (1982a), Measurement of fluid turbulence based on pulsed ultrasound techniques. Part 1. Analysis, *J. Fluid Mech.*, *118*, 445–470.
- Garbini, J. L., F. K. Forster, and J. E. Jorgensen (1982b), Measurement of fluid turbulence based on pulsed ultrasound techniques. Part 2. Experimental investigation, *J. Fluid Mech.*, *118*, 471–505.
- George, R., R. Flick, and R. Guza (1994), Observations of turbulence in the surf zone, *J. Geophys. Res.*, *99*(C1), 801–810.
- Gradshteyn, I. S., and I. M. Ryzhik (1980), *Table of Integrals, Series and Products*, Academic Press, New York, 1156 pp.
- Grant, W., and O. Madsen (1979), Combined wave and current interactions with a rough bottom, *J. Geophys. Res.*, *84*, 1797–1808.
- Grant, W., and O. Madsen (1982), Movable bed roughness in unsteady oscillatory flow, *J. Geophys. Res.*, *87*, 469–481.
- Grant, W., and O. Madsen (1986), The continental-shelf bottom boundary layer, *Ann. Rev. Fluid Mech.*, *18*, 265–305.
- Gross, T. F., A. J. Williams, and E. A. Terray (1994), Bottom boundary layer spectral dissipation estimates in the presence of wave motions, *Cont. Shelf Res.*, *14*, 1239–1256.
- Guza, R. T., and E. B. Thornton (1980), Local and shoaled comparisons of sea surface elevations, pressures and velocities, *J. Geophys. Res.*, *85*, 1524–1530.
- Hay, A., and T. Mudge (2005), Primary bed states during SandyDuck97: Occurrence, spectral anisotropy, and the bed state storm cycle, *J. Geophys. Res.*, *110*, C03013, doi:10.1029/2004JC002451.
- Hinze, J. O. (1975), *Turbulence*, second ed., McGraw-Hill, New York, 790 pp.
- Jonsson, I. (1966), Wave boundary layers and friction factors, in *Proc. 10th Coastal Eng. Conf.*, vol. 1, pp. 127–148, Am. Soc. Civ. Eng., New York.
- Kamphuis (1975), Friction factors under oscillatory waves, *J. Waterw. Harbours Coastal Eng.*, *101*, 135–144.
- Kundu, P. K. (1990), *Fluid Mechanics*, Academic Press, San Diego, 638 pp.
- Lumley, J. L., and E. A. Terray (1983), Kinematics of turbulence convected by a random wave field, *J. Phys. Oceanogr.*, *13*, 2000–2007.

- Madsen, O., P. Mathisen, and M. Rosengaus (1990), Movable bed friction factors for spectral waves, in *Proc. 22nd Coastal Eng. Conf.*, pp. 420–429, Am. Soc. Civ. Eng., New York.
- Monin, A. S., and A. M. Yaglom (1971), *Statistical Fluid Mechanics: Mechanics of Turbulence*, vol. 2, MIT Press, Cambridge, MA, 874 pp.
- Newgard, J. P., and A. E. Hay (2007), Turbulence intensity and friction in the wave bottom boundary layer under (mainly) flat bed conditions, *J. Geophys. Res.*, *112*, C09024, doi:10.1029/2006JC003881.
- Nielsen, P. (1981), Dynamics and geometry of wave-generated ripples, *J. Geophys. Res.*, *86*, 6467–6472.
- Nielsen, P. (1992), *Coastal Bottom Boundary Layers and Sediment Transport*, World Scientific, River Edge, New Jersey, 324 pp.
- Nuttall, A. H. (1971), Spectral estimation by means of overlapped fast fourier transform processing of windowed data, *Tech. Rep. 4169*, NUSC.
- Pope, S. (2000), *Turbulent Flows*, Cambridge Univ. Press, New York.
- Richardson, M. D., et al. (2001), Overview of SAX99: Environmental considerations, *IEEE J. Oceanic Eng.*, *26*(1), 26–53.
- Sleath, J. F. A. (1984), *Sea Bed Mechanics*, John Wiley, New York, 335 pp.
- Smyth, C., and A. E. Hay (2002), Wave friction factors in nearshore sands, *J. Phys. Oceanogr.*, *32*, 3490–3498.
- Smyth, C., and A. Hay (2003), Near-bed turbulence and bottom friction during SandyDuck97, *J. Geophys. Res.*, *108*(66), 3197, doi:10.1029/2001JC000952, 28–1–28–14.
- Swart, D. (1974), Offshore sediment transport and equilibrium beach profiles, *Tech. Rep. 131*, Delft Hydraulics Lab.
- Tennekes, H., and J. L. Lumley (1972), *A First Course in Turbulence*, MIT Press, Cambridge, MA, 300 pp.
- Thornton, E. B., and R. T. Guza (1983), Transformation of wave height distribution, *J. Geophys. Res.*, *88*, 5925–5938.
- Thorsos, E. I., and M. D. Richardson (2002), Guest editorial, *IEEE J. Oceanic Eng.*, *27*, 341–345.
- Thorsos, E. I., et al. (2001), Overview of SAX99: Acoustic measurements, *IEEE J. Oceanic Eng.*, *26*, 4–25.
- Tolman, H. (1994), Wind waves and moveable-bed bottom friction, *J. Phys. Oceanogr.*, *24*, 994–1009.
- Traykovski, P., A. E. Hay, J. D. Irish, and J. F. Lynch (1999), Geometry, migration, and evolution of wave orbital ripples at LEO-15, *J. Geophys. Res.*, *104*, 1505–1524.
- Trembanis, A. C., L. Wright, C. Friedrichs, M. Green, and T. Hume (2004), The effects of spatially complex inner shelf roughness on boundary layer turbulence and current and wave friction: Tairua embayment, New Zealand, *Cont. Shelf Res.*, *24*, 1549–1571.
- Trowbridge, J., and S. Elgar (2001), Turbulence measurements in the surf zone, *J. Phys. Oceanogr.*, *31*, 2403–2417.
- Veron, F., and W. K. Melville (1999), Pulse-to-pulse coherent Doppler measurements of waves and turbulence, *J. Atmos. Oceanic Technol.*, *16*, 1580–1597.
- Wiberg, P. L., and C. K. Harris (1994), Ripple geometry in wave-dominated environments, *J. Geophys. Res.*, *99*, 775–789.
- Wilson, K. (1989), Friction of wave-induced sheet flow, *Coastal Eng.*, *12*, 371–379.
- Zedel, L., and A. Hay (1999), A coherent Doppler profiler for high resolution particle velocimetry in the ocean: Laboratory measurements of turbulence and particle flux, *J. Atmos. Oceanic Technol.*, *16*(8), 1102–1117.
- Zedel, L., A. Hay, R. Cabrera, and A. Lohrmann (1996), Performance of a single beam, pulse-to-pulse coherent Doppler profiler, *IEEE J. Oceanic Eng.*, *21*(3), 290–297.

---

A. E. Hay, Department of Oceanography, Dalhousie University, Halifax, NS, Canada B3H 4J1. (alex.hay@phys.ocean.dal.ca)